Journal Name

ARTICLE TYPE

Cite this: DOI: 00.0000/xxxxxxxxxx

Quantum Stereodynamics of Cold Molecular Collisions

Naduvalath Balakrishnan[a], Pablo G. Jambrina[b], James F. E. Croft[c], Hua Guo[d], and F. Javier Aoiz[e]†

names go here instead of "Full name", etc.

Received Date
Accepted Date

DOI: 00.0000/xxxxxxxxxx

Advances in quantum state preparations combined with molecule cooling and trapping technologies have enabled unprecedented control of molecular collision dynamics. This progress, achieved over the last two decades, has dramatically improved our understanding of molecular phenomena in the extreme quantum regime characterized by translational temperatures well below a kelvin. In this regime, collision outcomes are dominated by isolated partial waves, quantum threshold and quantum statistics effects, tiny energy splitting at the spin and hyperfine levels, and long-range forces. Collision outcomes are influenced not only by the quantum state preparation of the initial molecular states but also by the polarization of their rotational angular momentum, i.e., stereodynamics of molecular collisions. The Stark-induced adiabatic Raman passage technique developed in the last several years has become a versatile tool to study the stereodynamics of light molecular collisions in which alignment of the molecular bond axis relative to initial collision velocity can be fully controlled. Landmark experiments reported by Zare and coworkers have motivated new theoretical developments, including formalisms to describe four-vector correlations in molecular collisions that are revealed by the experiments. In this Feature article, we provide an overview of recent theoretical developments for the description of stereodynamics of cold molecular collisions and their implications to cold controlled chemistry.

1 Introduction

Quantum control of molecular collisions and chemical reactions has long been a cherished goal of chemists and physicists alike. The advent of techniques to prepare atoms and molecules in well-defined quantum states and reduce their translational temperatures to well below a kelvin and even micro kelvin in some cases, has given rise to renewed interest in controlling chemical reactions in the ultimate quantum regime[1–8]. At low collision velocities corresponding to relative translational temperatures in the mK and K range the de Broglie wave lengths become much larger than inter-particle separations and quantum effects become amplified. The experimental techniques that led to the creation of Bose-Einstein condensates of alkali-metal atoms have expanded into a flourishing area of research that overlaps chemistry, physics and astrophysics. In particular, creation of ultracold molecules via photoassociation[9] or magnetoassociation[10,11] of ultracold atoms or via direct cooling of pre-existing molecules through buffer-gas cooling[12–14], Stark or Zeeman deceleration[15–17] and laser cooling[18,19] has opened up exciting opportunities to probe molecular collisions and chemical reactions with energy and quantum-state resolution that were not possible until recently. These developments have led to state-resolved studies of ultracold chemical reaction such as KRb+KRb K_2+Rb_2 at temperatures of about 400 nK[6,7]. Because the KRb molecule with ^{40}K and ^{87}Rb is a composite fermion, the lowest allowed partial wave is a p-wave for collisions between two KRb molecules in the same internal state. The reaction still occurs by tunneling through the p-wave barrier at a collision energy of about 350 nK with a rate coefficient of about $10^{\;11}$ cm^3/s. If the two KRb molecules are prepared in different hyperfine states then s-wave scattering is allowed leading to an order of magnitude larger value for the reaction rate, due to the absence of centrifugal barrier[20]. A comparable value was also reported for the K+KRb K_2+Rb reaction[20] though these experiments were not able to measure the quantum states of the reaction products. Alkali metal systems are very challenging for theoretical calculations employing an explicit quantum mechanical approach. While computations have been reported for KRb+K[21,22] and Li+LiNa[23,24], they are challenging especially

---

[a] Department of Chemistry and Biochemistry, University of Nevada, Las Vegas, Nevada 89154, USA.
‡ E-mail: naduvala@unlv.nevada.edu
[b] Departamento de Química Física, Universidad de Salamanca, Salamanca 37008, Spain
[c] The Dodd Walls Centre for Photonic and Quantum Technologies, New Zealand and Department of Physics, University of Otago, Dunedin, New Zealand
[d] Department of Chemistry and Chemical Biology, University of New Mexico, Albuquerque, New Mexico 87131, USA.
[e] Departamento de Química Física, Universidad Complutense, Madrid 28040, Spain

for the heavier alkali metal systems and when non-adiabatic effects need to be taken into account. For the KRb+KRb system full quantum calculations incorporating spin and hyperfine effects and resolution of the product quantum states are not currently feasible. Clearly, new methodologies are needed to tackle these systems. Here we focus on light molecular systems for which explicit quantum calculations can be carried out.

The Stark-induced adiabatic Raman passage (SARP) technique introduced by Mukherjee, Zare and coworkers[25–36] provides an ideal platform to study cold collisions of light molecular systems such as H_2 and its isotopologues. These systems allow explicit quantum calculations on highly accurate interaction potentials and direct comparisons with experiments. In the approach developed by Zare and coworkers the colliding species are co-expanded in a supersonic molecular beam and the SARP lasers excite the molecule into a chosen rovibrational level (v j) with a particular polarization of the rotational angular momentum. Using this technique, v, j, and its projection on a space-fixed (laboratory) axis (m_j) can be selected. In addition, changing the direction of the polarization vector with respect to the relative velocity makes it possible to select the initial alignment of the molecular bond axis relative to the scattering frame. This allows stereodynamics of molecular collisions involving state-prepared and aligned molecules be probed and controlled. The method has been applied to rotational quenching of HD by D_2, H_2[28,29], He[30,35] and of D_2 by He[32,33], Ne[34] and D_2[36] at cold temperatures. In the latter case aligned-aligned collisions of two D_2 molecules were studied for the first time. Unlike ultracold collisions that are sensitive to the long-range part of the interaction potential, SARP techniques can access collision energies in the 1 K regime and also probe the anisotropic part of the interaction potential. For systems with interaction potential strength on the order of 10-100 K, shape resonances generally occur in the 1 K regime making the SARP techniques ideal for sensitive probe of the interaction potential.

Details of the SARP method and its applications to rotational quenching in atom-diatom and diatom-diatom collisions have recently been reviewed by Mukherjee[37]. Here, we focus on the theoretical work motivated by experiments in which the alignment of the molecular axis can be selected and varied[38–49]. The paper is organized as follows. In Section 2 we review some pertinent work related to the stereodynamics of molecular collisions that were reported prior to the development of the SARP method as well as recent experimental progress in cold collisions. In Section 3, we provide a brief description of the SARP method and the theoretical formalism to describe the SARP experiments. In Section 4 we provide illustrative results of molecule-molecule collisions considering the polarization of one or both molecules and how three- or four-vector correlations in molecular collisions can be extracted. Atom-diatom inelastic collisions are discussed in Section 5 while reactive collisions are discussed in Section 6. Recent theoretical progress in applying SARP methods to polyatomic molecules is reviewed in Section 7. Finally, Section 8 provides an outlook for future studies, including coherent control of molecular collisions and chemical reactions with stereodynamically prepared molecules.

2 Background

Rotationally resolved cross sections and rate coefficients for inelastic and reactive collisions from molecular beam experiments usually involve a sum of over the magnetic projection quantum numbers (m_j) of the products and an average over m_j for rotational level j of the reactants. However, m_j-resolved cross sections can provide useful information on the anisotropy of the interaction potential. By selecting the magnetic sub-levels of a given rotational level one can control the initial alignment and orientation of the reactants and explore intimate details of the collision dynamics and possibly control the reaction outcome. For early experimental and theoretical analysis of polarized collisions in atom-molecule systems, we refer to the work of Herschbach and coworkers[50–52], Alexander et al.[53], and Orr-Ewing and Zare[54]. More recently, Aoiz and coworkers[55–58] have discussed angular momentum distributions in quantum and classical descriptions of molecular collisions. In particular, they have analyzed how reactant polarization controls product angular distributions and presented a formalism to calculate polarization dependent-differential cross sections (PDDCSs)[56,59,60]. Aldegunde et al. applied the scheme to the stereodynamics of the benchmark $D+H_2$[57], $H+D_2$[61] and $F+H_2$ $HF+H$[62,63] chemical reactions and illustrated that the reactivity can be controlled to a considerable extent through alignment of the rotational angular momentum of the H_2 molecule. Previously, Balakrishnan and Dalgarno[64] have shown that the $F+H_2$ reaction may occur with a rate coefficient on the order of 10 ^{12} cm^3/s in the ultracold limit.

In the last quarter century, as techniques to create cold and ultracold molecules as well as methods to cool and trap atoms, ions, and molecules have proliferated[1–7], controlled studies of reactive and inelastic molecular collisions have become a frontier area of research. However, state-to-state chemistry in the ultracold regime is a challenging task experimentally due to the difference in energy-scale involved for the relative motion in the reactant and product channels and the large energy released compared to the trapping potential. As a result, until recently, only the total decay rate was typically reported by considering the loss rate of the reactants rather than measuring the product quantum states. Such reaction rates were reported for the KRb+KRb K_2+Rb_2 and K+KRb K_2+Rb chemical reaction by Ospelkaus et al. in 2010[20,65]. Recently, Ni and co-workers[66–68] reported the first state-to-state measurements of the rate of KRb+KRb chemical reaction using velocity map imaging (VMI) of the K_2 and Rb_2 products. Product detection is facilitated in this case due to the modest 10 K exoergicity which limits the number of K_2 and Rb_2 rotational pairs to 57, all in the ground vibrational level. The experiment also revealed that the reaction occurs through an intermediate K_2Rb_2 complex that lies at an energy close to that of the reactant molecules, also detected using the VMI technique. Full quantum calculations of reactive scattering such as KRb+KRb K_2+Rb_2 are currently not possible due to the large number of internal states of the KRb, K_2, and Rb_2 molecules as well as that of the tetramer complex that need to be taken into account in a quantum mechanical description. Thus, simplified methods based on multichannel quantum defect theory for total reaction rates [69,70] or statistical quantum approaches [71–73] are adopted. The latter can yield state-to-state rate coefficients but its accuracy hedges on the full randomization of the vibrational energy in the reaction intermediate.

While alkali metal dimer systems continue to attract a great deal of interest in quantum science applications benchmark calculations are more challenging for these systems. Full-dimensional quantum calculations of atom-dimer and dimer-dimer collisions are still largely limited to H_2 and light molecules containing hydrogen atoms. However, molecules such as H_2, CO, HCl, HF, O_2, OH, etc. are more difficult to cool and trap compared to alkali metal systems but are more chemically interesting and amenable to numerically exact quantum calculations. Some of these systems are also of considerable interest in astrophysics and extensive quantum calculations of rovibrational transitions in CO induced by H_2 and He have been reported [74–78]. Rotational quenching and excitation in CO and O_2 by collisions with He and H_2 have been the topic of several experiments in recent years using cryogenic techniques at temperatures as low as 5 K [79,80]. Quantum close-coupling calculations were highly successful in reproducing the experimental results that also revealed narrow resonances in the energy dependence of the rotational excitation cross sections [74,76,77,79,80].

Recently Perreault et al. [27–31] and Zhou et al. [32,33,36,37] demonstrated that one can study cold collisions in intrabeam scattering without actually cooling or trapping the collision partners. The technique first demonstrated by Suits and coworkers [81,82] for atom-atom collisions involves co-expanding the collision partners in the same molecular beam. While the velocities of each species are high in the laboratory frame, small relative velocities can be achieved enabling cold collisions in the 1 K regime. Mukherjee and collaborators combined this technique with the SARP technique to study the stereodynamics of cold molecular collisions. The SARP technique allows preparing the molecules in a chosen v, j, and m_j quantum numbers so as to enable alignment of one or both collision partners relative to the initial polarization of the SARP laser. For example, for the j 2 rotational level, a horizontal alignment of the molecular bond axis relative to the initial velocity vector corresponds to m_j 0 while a vertical alignment corresponds to a superposition of m_j states with contributions from m_j 0, and m_j 2. By taking appropriate linear combination of m_j states, an arbitrary alignment of the bond axis relative to the initial relative velocity vector can be prepared allowing stereodynamic control of the collision process. They have demonstrated this approach to rotational quenching of HD(v j) in collisions with H_2, D_2 and He [27–31] and more recently collisions of two aligned D_2 molecules [36]. For these molecular systems, collisions are dominated by a few partial waves in the vicinity of 1 K revealing signatures of isolated partial waves in the measured angular distribution. However, the experimental collision energy distribution is relatively broad, which makes theoretical studies necessary to evaluate partial wave resolved cross sections and identify features of the measured differential cross sections (DCSs) arising from specific angular momentum partial waves. Below we will highlight some of these studies for both atom-dimer and dimer-dimer collisions and compare with experimental data. Comparisons with experiments also reveal that even for simple 4-electron systems such as He+HD and He+D_2, experiment and theory do not always agree. The lack of agreement may reflect small errors in the state-of-the-art interaction potentials leading to different collision outcomes in the sub kelvin and kelvin ranges of collision energies, or perhaps inaccuracies in the experimental collision energy resolution.

3 Theory

3.1 Three-vector correlations in collisions of a polarized and an unpolarized diatomic molecule

First, we briefly review the theoretical formalism describing the stereodynamics of molecule-molecule collisions for the case where only one of the collision partners is polarized (for example **1**). This would correspond to a three-vector correlation, i.e., alignment of the initial rotational angular momentum $\boldsymbol{j}$ of the polarized molecule and the initial and final relative velocity vectors, respectively, $\boldsymbol{k}$ and $\boldsymbol{k}$. Note that in the center-of-mass frame, the scattering angle is the angle between $\boldsymbol{k}$ and $\boldsymbol{k}$ and the quantization axis z is oriented along $\boldsymbol{k}$. We use the notation $v_1\ j_1\ v_2\ j_2$ to denote the initial combined molecular states and $v_1\ j_1\ v_2\ j_2$ to denote the corresponding quantum numbers after the collision. The scattering amplitude for a $m_1\ m_2$) to $m_1\ m_2$) transition, where m_1 and m_2 are the projections of the initial rotational levels of the two molecules with the primed quantities denoting the final states, is expressed in terms of the corresponding T-matrix elements [38,39,46,49],

$$f \quad {}_{m_1 m_2} \quad {}_{m_1 m_2} \quad \frac{1}{2k} \quad {}_J \; 2J \quad 1 \quad {}_{j_{12}\, j_{12}\, L\, L} \; i^{L \;\; L \;\; 1} d^J_{m_{12}\, m_{12}}$$

$$T^J{}_{L j_{12} \quad L\, j_{12}} \; j_{12} m_{12}\; J \quad m_{12}\; L\, 0 \quad j_{12} m_{12}\; J \quad m_{12}\; L0 \tag{1}$$

$$j_1 m_1\; j_2 m_2\; j_{12} m_{12} \quad j_1 m_1\; j_2 m_2\; j_{12} m_{12}$$

where m_{12} m_1 m_2, m_{12} m_1 m_2, is the scattering angle, $d^J_{m_{12}\ m\ 12}$ is a Wigner's reduced rotation matrix, and is a Clebsch-Gordan coefficient. Also, k^2 2 E_{coll} $\hbar^2$ is the square of the wave vector in channel , E_{coll} is the collision energy, is the reduced mass, T^J 1 S^J, j_{12} j_1 j_2, L is the orbital angular momentum quantum number, and J the total angular momentum quantum number where J L j_{12}. The DCS for isotropic scattering is given by

$$\frac{d}{d} \quad \frac{1}{2j_1 \quad 1 \;\; 2j_2 \quad 1} \; {}_{m_1\, m_2\, m_1\, m_2} \; f \quad {}_{m_1 m_2} \quad {}_{m_1 m_2} f \quad {}_{m_1 m_2} \quad {}_{m_1 m_2} \tag{2}$$

where is the solid angle. The DCS includes interferences (coherences) between all J involved. Integration of the DCS over the solid angle washes out all interference terms, so the corresponding integral cross section (ICS) for state-to-state rovibrationally inelastic scattering is given by

$$\frac{}{2j_1 \quad 1 \;\; 2j_2 \quad 1\; k^2} \; {}_{J\, j_{12}\, j_{12}\, L\, L} \; 2J \quad 1 \;\; T^J{}_{L j_{12} \quad L\, j_{12}}{}^2 \tag{3}$$

As a consequence of these interference terms, it is not guaranteed that the DCS for a given will increase upon the addition of more partial waves. In fact, partial waves that barely contributes to the ICS may dramatically change the shape of the DCS as shown for reactive collisions between H and D_2 at high energies.[83–85] To disentangle the partial waves that contribute to the scattering at a given angle as well as the interference between groups of partial waves, it is desirable to calculate the generalized deflection function (GDF). The GDF is the joint quasi-probability density function of J and , allowing us to display the cross section in a J map. Following Refs. 86,87, the GDF ($Q_r \quad J$) can be defined as:

$$Q_r \quad J \qquad \frac{\sin}{2j_1 \quad 1 \quad 2j_2 \quad 1} \quad {}_{m_1 m_2 m_1 m_2 \; J_1 \quad 0 J_2 \quad 0}^{J_{\max} \; J_{\max}} \frac{\left(\; J_1 J \qquad J_2 J \right)}{2}$$

$$f^{J_1}{}_{m_1 \, m_2 \qquad m_1 \, m_2} f^{J_2}{}_{m_1 \, m_2 \qquad m_1 \, m_2} \tag{4}$$

where $f^J{}_{m_1 \, m_2 \qquad m_1 \, m_2}$ the J-dependent partial scattering amplitude such that

$$f \;{}_{m_1 \, m_2 \qquad m_1 \, m_2} \qquad {}_J \, f^J{}_{m_1 \, m_2 \qquad m_1 \, m_2} \tag{5}$$

In subsequent discussions, for simplicity, we will suppress the indices and on the scattering amplitudes but their presence is implied. Aoiz and coworkers have shown that the intrinsic PDDCSs are convenient means of describing vector correlations (stereodynamics) in molecular collisions[56–58]. For example, three-vector $\boldsymbol{k}$-$\boldsymbol{j}_1$-$\boldsymbol{k}$ correlations with rank k and component q in molecule-molecule collisions can be expressed as:

$$U_q^k \qquad \frac{1}{2j_1 \quad 1 \quad 2j_2 \quad 1} \;{}_{m_1 \, m_2 \, m_1 \, m_2} \quad f_{m_1 \, m_2 \quad m_1 \, m_2} f_{m_1 \quad q \, m_2 \quad m_1 \, m_2}$$

$$j_1 m_1 \;\; kq \;\; j_1 m_1 \quad q \tag{6}$$

where the $q \quad 0$ terms accounts for coherences between states with different m_1.

As discussed by Aldegunde et al.[57] for a reactant molecule prepared in a state, $j \quad m \quad 0$, its internuclear axis can be aligned along the quantization axis in the laboratory fixed frame coincident with the light polarization vector. Considering that the scattering frame is defined by $\boldsymbol{k}$ and $\boldsymbol{k}$ the internuclear axis distribution for a given preparation is given by[57]

$$P \quad {}_r \quad {}_r \qquad \frac{1}{4} \;{}_{k \;\; q \quad k}^{\quad k} \quad 2k \quad 1 \left[\mathscr{A}_0^{\,k} \, C_{kq} \qquad \right] C_{kq} \quad {}_r \quad {}_r \tag{7}$$

where C_{kq} (and $C_{kq} \quad {}_r \quad {}_r$) are modified spherical harmonics and $\mathscr{A}_0^{\,k} \qquad j_1 0 k 0 \; j_1 0$ are the extrinsic polarization parameters that define the preparation in the laboratory frame. The angles and are the polar and azimuthal angles that define the direction of the laboratory quantization axis with respect to the scattering frame while ${}_r$ and ${}_r$ define the direction of the relevant internuclear axis in the scattering frame. The polarization parameters for nonzero values of q are given by

$$a_q^k \quad C_{kq} \qquad \mathscr{A}_0^{\,k} \tag{8}$$

In terms of the three-vector PDDCSs U_q^k and the polarization parameters $\mathscr{A}_0^{\,k}$, one can express the DCS for a given preparation of $\boldsymbol{j}_1$ as[46]

$$\frac{d}{d} \qquad {}_{k \;\; 0 q \quad k}^{2j_1 \quad k} \quad 2k \quad 1 \, \mathscr{A}_0^{\,k} \, U_q^k \quad C_{kq} \tag{9}$$

When integrating over the azimuthal angle (or) all terms with $q \quad 0$ vanish. Further integration of the DCS over the scattering angle yields the alignment ( )-dependent ICS.

It is also possible to use the GDF formalism to disentangle the contribution for each partial wave to the DCS calculated from a given preparation:[87]

$$Q \quad J \quad \frac{\mathrm{iso}}{2} \;{}_{k \;\; q \quad k}^{\quad k} \quad 2k \quad 1 \left[Q_q^k \qquad J \right] A_q^k \, C_{kq} \tag{10}$$

where ${}_{\mathrm{iso}}$ is the isotropic ICS and

$$Q_q^k \quad J \qquad \frac{\sin}{2j_1 \quad 1} \;{}_{m_1 m_2 m_2 \;\; J_1 \quad 0 J_2 \quad 0 \; m_1}^{J_{\max} \; J_{\max}} \frac{\left(\; J_1 J \qquad J_2 J \right)}{2}$$

$$f^{J_1}_{m \, m} \, f^{J_2}_{m \, m \quad q} \quad jm_1 \;\; kq \;\; jm_1 \quad q \tag{11}$$

In Fig. 1 we show the isotropic and $\quad 0$ DCSs for the H + D_2 (v=0,j=2) HD(v =1,j =0) + D reaction at E_{coll}=1.97 eV[87]. The isotropic and, especially, the $\quad 0$ DCSs feature a series of peaks and dips. Inspection of the quantum mechanical (QM) GDF in the bottom panel allows us to conclude that, for $\quad 0$, the most backward peak is caused by $J \quad 0 \quad 15$, the second peak comes from $J \quad 20$, the third peak, at 115 , originates from two separate groups of J, while the minimum at 135 is caused by the destructive interference between $J \quad 10$ and $10 \quad J \quad 25$ (as depicted by the green area).

3.2 Four-vector correlations in collisions of two polarized molecules

If both molecules are polarized under the same polarization vector, then the DCS can be expressed as [49]

$$\frac{d}{d} \qquad {}_{k_1 \quad 0 \, q_1 \; k_2 \quad 0 \, q_2}^{2j_1 \qquad 2j_2} \quad 2k_1 \quad 1 \quad 2k_2 \quad 1$$

$$\left[U_{q_1 \, q_2}^{k_1 \, k_2} \qquad \right] a_{q_1}^{k_1} \, a_{q_2}^{k_2} \tag{12}$$

where each of the a_q^k can be evaluated according to Eq. (8) as a function of the and angles. The intrinsic {$\boldsymbol{k}$–$\boldsymbol{j}_1$–$\boldsymbol{j}_2$–$\boldsymbol{k}$ } 4-vector

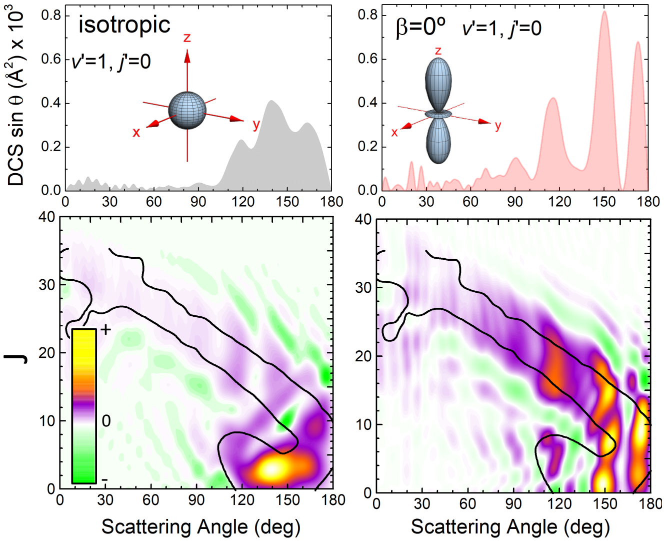

Fig. 1 Differential cross sections for the H + D$_2$ (v=0, j=2) HD(v =1, j =0) + D reaction at $E_{\rm coll}$=1.97 eV for an isotropic preparation (left panel) and for 0 (right panel). The QM GDFs for the isotropic preparation and polarized reactants are shown in the bottom panels. The green zones correspond to destructive interference (those partial waves that deplete scattering at a given angle). Adapted with permission from[87], 2019, Royal Society of Chemistry.

PDDCSs, $U_{q_1\ q_2}^{k_1\ k_2}$, can be calculated as [49]

$$U_{q_1\ q_2}^{k_1\ k_2} \qquad \frac{1}{2j_1 \quad 1\ \ 2j_2 \quad 1} \tag{13}$$

$$\sum_{\substack{m_1\ m_2\\ m_1\ m_2}} f_{m_1m_2} \quad m_1 m_2 \qquad f_{m_1m_2} \quad m_1 \quad q_1 \quad m_2 \quad q_2$$

$$j_1m_1\ k_1q_1\ j_1\ \ m_1 \quad q_1 \qquad j_2m_2\ k_2q_2\ j_2\ \ m_2 \quad q_2$$

If either k_1 or k_2 is zero, we recover the three-vector PDDCS U_q^k . If k_1 k_2 0 we recover the U_0^0 , the isotropic DCS.

4 SARP Preparation and diatom-diatom inelastic collisions

In the SARP technique, a polarized molecule with angular momentum vector $\boldsymbol{j}$ is prepared in a state $j\ \tilde{m}\quad 0$ in which the quantization axis of $\tilde{m}$ is determined by the alignment of the linear polarization of the SARP laser. The alignment angle can be chosen as the angle between the linear polarization of the SARP laser and the beam velocity in the laboratory frame. In this way, a state of a molecule prepared in a non-zero rotational state $j\ \tilde{m}$ may be expressed as[39]

$$j\ \tilde{m} \qquad \sum_{m \quad j}^{j} d_{\tilde{m}\,m}^{j} \qquad j\ m \tag{14}$$

where m is the projection of j on the initial relative relative velocity vector which is directed along the beam velocity (z-axis). Here we consider only states prepared in the SARP experiments that corresponds to $\tilde{m}$ 0. For j=2, the experiments considered three specific preparations: H-SARP (pure m 0), a bi-axial state

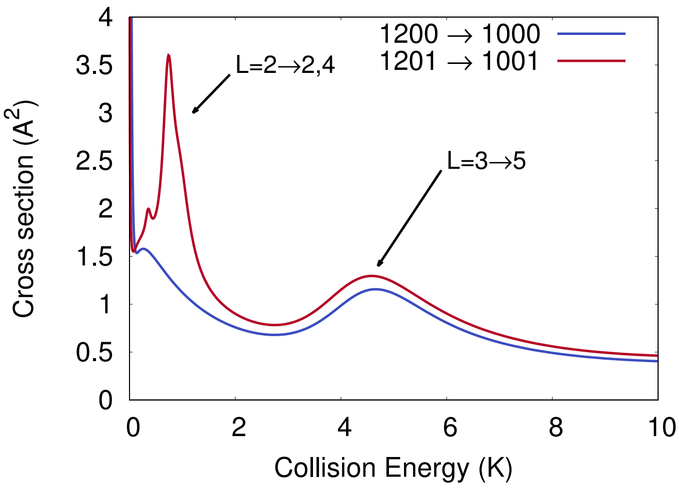

Fig. 2 Integral cross sections for j 2 rotational quenching in HD v_1 1 j_1 2 in collisions with H$_2$ as a function of the collision energy. The red curve is for ortho-H$_2$ and the blue curve is for para-H$_2$ with the numbers denoting combined molecular states and . The values of the partial wave (L) associated to the resonances are highlighted in the figure. Reproduced with permission from[38], 2018, American Physical Society.

X-SARP (a linear combination of m 1), and V-SARP (a linear combination m 0 2)[37]. In particular, for j=2 the V-SARP preparation corresponds to

$$\sqrt{\frac{3}{8}}\ \ j_1 \quad 2\ m_1 \qquad 2 \qquad j_1 \quad 2\ m_1 \quad 2 \qquad \frac{1}{2}\ j_1 \quad 2\ m_1 \quad 0 \tag{15}$$

where we have assumed molecule 1 with angular momentum $\boldsymbol{j_1}$ is polarized. When integrated over the azimuthal angle , the DCS for a given SARP preparation is given by[39]

$$\frac{d}{d} \qquad \frac{2\ \ \sin}{2j_2 \quad 1} \tag{16}$$

$$\sum_{m_1\ m_2\ m_1\ m_2} d_{0\ m_1}^{j_1} \qquad ^2\ f_{m_1\ m_2\ m_{12}} \quad m_1\ m_2\ m_{12} \quad ^2$$

Note that the interference term between different initial m-states in the SARP preparation drops off up on integrated over [39]. Below we provide some illustrative results of stereodynamic control of cold molecular collisions and compare with available experimental data.

4.1 Cold collisions of aligned HD with H$_2$ and D$_2$

Perreault et al. reported the effect of the SARP preparation on the rotational quenching of HD(v_1 1 j_1 2 in collisions with H$_2$ and D$_2$.[28,29] Both H-SARP and V-SARP preparations of the HD molecule were considered while H$_2$/D$_2$ were unpolarized. For details of the experiments including the initial velocities of the two molecules as well as the relative velocities for the collision we refer to the experimental work. To simulate the measured DCS for H$_2$ collisions, quantum close-coupling calculations were reported by Croft et al.[38] using the formalism discussed in section 3.1 and the six-dimensional ab initio potential

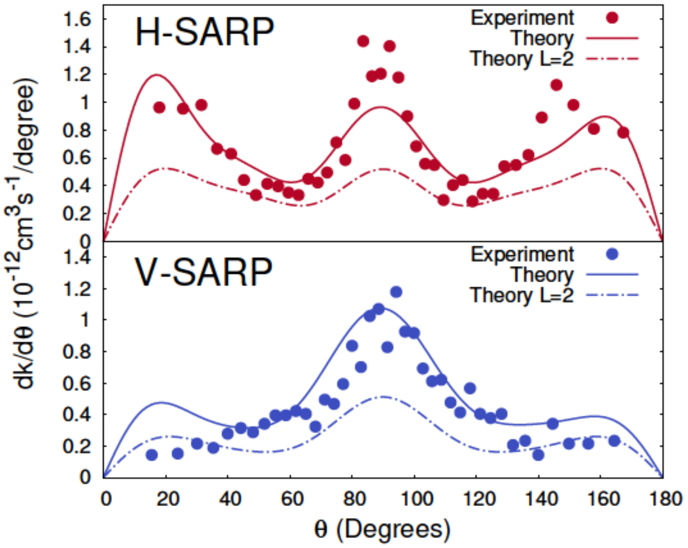

Fig. 3 Velocity averaged differential cross sections for rotational quenching in HD($v_1 = 1, j_1 = 2$)+H_2 collisions for H-SARP and V-SARP alignments of the HD molecule. The experimental data are shown by filled circles while the computed results are denoted by solid curves. The dashed curves show results from a calculation considering only the $L = 2$ contribution. Reproduced with permission from [38] 2018, American Physical Society.

energy surface (PES) of Hinde[88]. Figure 2 shows the isotropic ICS for HD($v_1 = 1, j_1 = 2$)+H_2 → HD($v_1' = 1, j_1' = 0$)+H_2[38] collisions. Both *ortho*-H_2($j_2 = 1$) and *para*-H_2($j_2 = 0$) collisions were considered. It can be seen that *ortho*-H_2 collisions dominate the cross sections and feature a strong $L = 2$ partial wave resonance near 1 K. This feature is absent in *para*-H_2 collisions. A weaker $L = 3$ resonance occurs in both *ortho*− and *para*−H_2 collisions near 4 − 5 K. Because of the higher statistical weight of ortho-H_2, the DCS is dominated by the $L = 2$ resonance in *ortho*-H_2 collisions. Figure 3 shows a comparison between the experimental and theoretical simulations of the SARP DCSs for both H-SARP and V-SARP preparations[38]. It is seen that theory can account for the key features of the experimental DCS, with the dominant contribution coming from the $L = 2$ partial wave resonance. We note that the experimental velocity distribution includes both the $L = 2$ and $L = 3$ resonance regions but cannot resolve specific resonances. Theory is therefore needed to disentangle the main features of the experimental angular distribution and to ascribe them to main partial wave contributions.

The experimental study of HD($v_1 = 1, j_1 = 2$)+H_2 collisions were limited to $\Delta j = -2$ transition in HD leading to the HD($v_1 = 1, j_1 = 0$) product. However, theoretical investigations of Jambrina et al.[40] revealed striking differences in the ICS for different SARP preparations for $\Delta j = -1$ and $\Delta j = -2$ transitions in HD. This is illustrated in Fig. 4 where the ICS for different alignment angles β are shown[40]. It is seen that a strong resonance feature occurs in the $\Delta j = -1$ case near a collision energy of 0.1 K that is sensitive to the alignment angle. This feature is present for $\beta = 90°$ and magic angle (∼ 54.7°, the one for which the second-order Legendre polynomial is zero) as well as isotropic scattering. However, it is entirely absent for $\beta = 0°$ (H-SARP preparation). On the other hand, there is no resonance at 0.1 K for $\Delta j = -2$. Thus, for a given Δj transition, stereodynamic preparation can strongly influence resonance features in ICS, not merely the angular distribution. Figure 5 provides further insights into how the collision geometry changes as the collision energy approaches the resonance region for the $\Delta j = -1$ transition[40]. This is obtained by examining the polarization parameters $U_q^k(\theta)$ that provide the internuclear axis distribution, essentially a "stereodynamical portrait" of the collision process.[56] It is seen that, at low collision energies just below the resonance, the collision occurs primarily "head-on" but it changes to a "side-on geometry" (internuclear axis perpendicular to the z-axis) at the resonance energy. At energies above the resonance, no preferred orientation is seen.

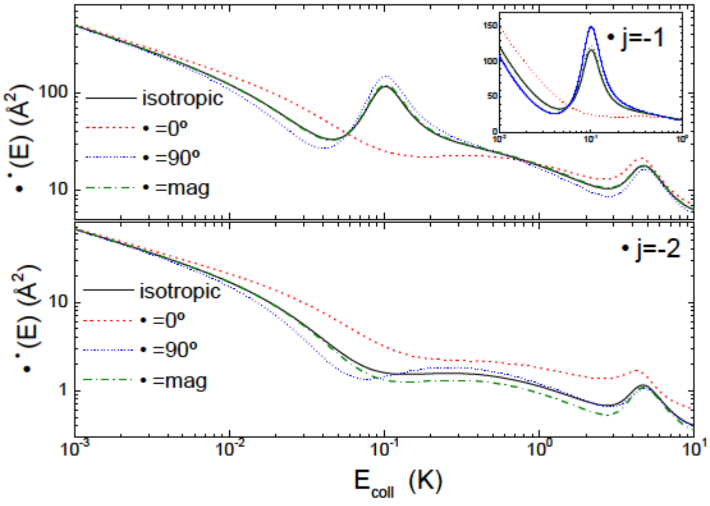

Fig. 4 ICS vs collision energy showing alignment effects in rotational quenching of HD($v = 1, j = 2$) by collisions with H_2. Results are depicted in a logarithmic scale. To highlight the effect of the alignment around the resonance, the inset shows the resonance region in a linear ordinate-axis scale. Reproduced with permission from [40] 2019, American Physical Society.

4.2 Cold collisions of aligned HCl with H_2

Marked stereodynamic control of cold collisions of SARP prepared HCl with H_2 has also been observed at the level of ICS[44]. This system is more anisotropic than that of HD-H_2 and exhibits more resonance features in the ICS at collision energies near and below 1 K. While no SARP experiments in a single beam have been reported on this system, the cross sections are dominated by a few partial waves allowing almost complete control of the resonance features through stereodynamic preparations. Figure 6 illustrates strong modulations in the ICS for $\Delta j = -2$ rotational quenching of HCl($v_1 = 1, j_1 = 2$) by collisions with para-H_2 near a collision energy of 0.3 cm^{-1} due to a $L = 1$ partial wave resonance[44]. The resonance is strongly enhanced by the H-SARP preparation and $\beta = 10°$ and 30° while $\beta = 50°$ yields nearly the same cross sections as in isotropic collisions. The V-SARP preparation on the other hand yields the lowest cross section. Thus, the resonance can be completely "switched off" or enhanced through stereody-

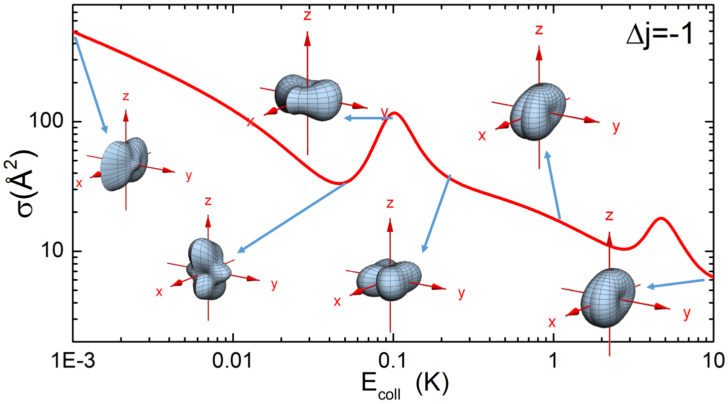

Fig. 5 Integral cross section for j 1 rotational quenching of HD(v 1 j 2) by collisions with H_2 along with stereodynamical portraits of the collision dynamics. The z axis is parallel to $\boldsymbol{k}$, the x-z plane is the scattering plane, and the y axis is parallel to $\boldsymbol{k}$ $\boldsymbol{k}$. Reproduced with permission [40] 2019, American Physical Society.

namic preparations allowing full control of the reaction dynamics in the vicinity of the resonance. For the j 1 transition the resonance profile is somewhat changed with the L 1 resonance pushed to around 0.15 cm ^{1} while a new L 3 resonance appears at around 0.4 cm ^{1}. These two resonances have some overlaps as the p-wave resonance has a non-zero contribution in the region of the f-wave resonance. The question then is can one control the intensities of the two resonances through stereodynamic preparation? This is illustrated in Fig. 7 where strong control of the two resonances is seen for different alignments[44]. In this case, it is the H-SARP preparation that suppresses the resonances while the V-SARP preparation enhances both. That stereodynamic preparations can simultaneously control multiple resonances bode well for quantum control of molecular collisions.

4.3 Cold collisions of aligned CO with HD

Rotational de-excitation of stereodynamically prepared HD(v 0 j 2) by CO also reveals strong stereodynamic effect[46]. In this case, both j 1 and j 2 transitions in HD can lead to rotational excitation of the CO molecule. This system reveals more complicated dynamics due to simultaneous rotational transitions in both molecules and the contributions from more than one partial wave in the resonance region. This is illustrated in Fig.8 that shows the energy dependent ICS for the different final states in HD(v_1 0 j_1 2)+CO(v_2 0 j_2 0 HD(v_1 0 j_1)+CO(v_2 0 j_2) collisions[46]. It is seen that 0 (H-SARP) leads to the lowest cross sections in the resonant region centered around 0.1 K except for j_2 0 for CO. For all other final rotational levels of CO 90 and =magic angle yield the highest cross sections. Figure 9 provides L-resolved cross sections for HD(j_1 1) and CO(j_2 3) for different values[46]. It is seen that both L 1 and L 2 contribute to the resonance and the relative contributions of the two partial waves depend strongly on the alignment. As discussed in detail by Jambrina et al.[46] parity conservation also strongly influences the relative contributions from the two partial waves which can arise from different values of

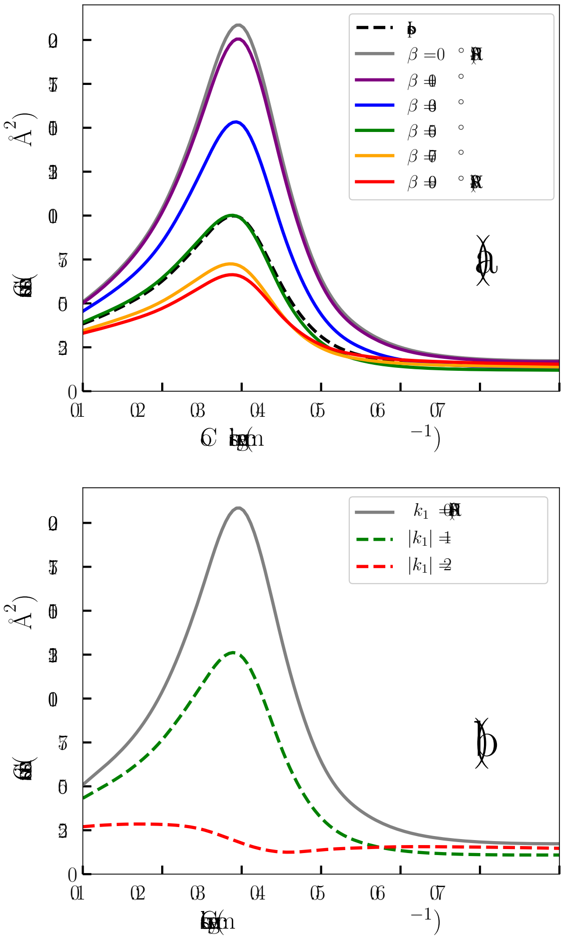

Fig. 6 Panel (a): ICS as a function of the collision energy for different alignment angles of HD bond axis illustrating stereodynamic effect in j 2 rotational quenching of HCl(v 1 j 2) by collisions with H_2. Panel (b): contributions from different orientations specified by quantum number k_1, the projection of the initial rotational angular momentum of HCl onto the body-fixed z-axis. The result for k_1 0 is identical to 0 (H-SARP) in panel (a). Reproduced with permission from [44], 2020, American Physical Society.

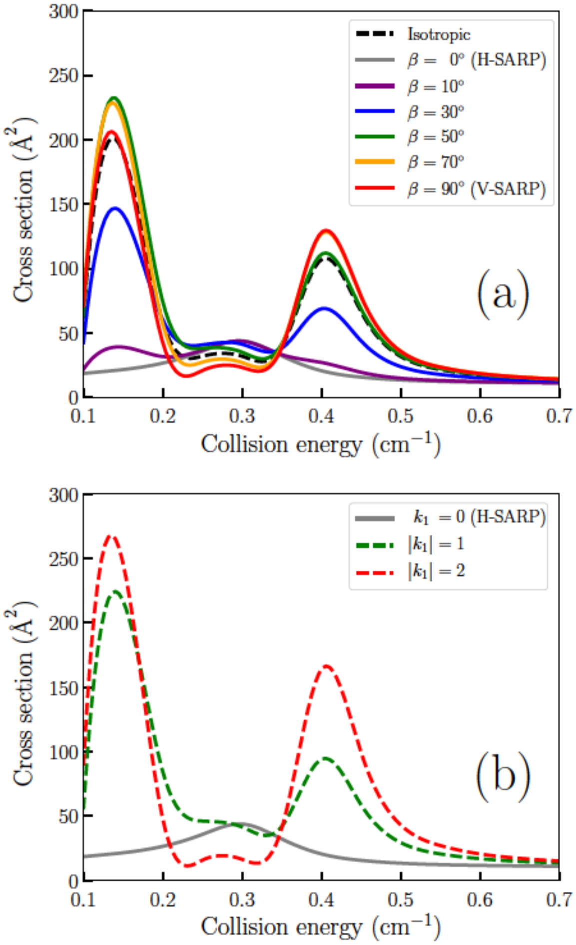

Fig. 7 Same as in Fig. 6 but for $\Delta j = -1$ transition in HCl($v = 1, j = 2$) + H_2 collisions. Reproduced with permission from [44], 2020, American Physical Society.

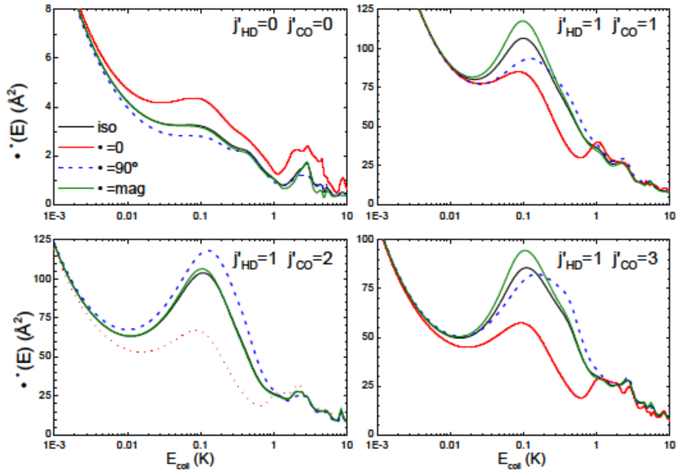

Fig. 8 Alignment effects in collision energy vs ICS in rotational quenching of HD($v = 1, j = 2$) by CO($v = 0, j = 0$) for different final rotational levels of the two molecules. Reproduced with permission from [46], 2021, Royal Society of Chemistry.

the total angular momentum quantum number that is conserved in the collision. We hope experimental studies of these intricate stereodynamic effects will be undertaken in the near future.

4.4 Cold collisions of two aligned D_2 molecules

Zhou et al.[36] have recently reported experimental results of stereodynamic effects in collisions of two aligned D_2 molecules prepared in the $v = 2, j = 2$ initial state. Results show that H-SARP and V-SARP preparations yield distinct angular distributions with strong forward and backward scattering peaks observed for H-SARP and a dominant peak centered around $\theta = 90°$ for the V-SARP case. A quantitative description of these experiments requires a formalism to extract $\boldsymbol{k}$-$\boldsymbol{j_1}$-$\boldsymbol{j_2}$-$\boldsymbol{k'}$ four-vector correlations. By applying the formalism for aligned-aligned collisions discussed in section 3.2 and the recently computed H_4 PES of Zuo et al.[89] that can describe collisions of highly vibrationally excited H_2 molecules, Jambrina et al.[49] carried out a full ab initio simulation of this process. The simulation includes collisions of two aligned D_2 molecules prepared in the $v = 2, j = 2$ level as well as aligned-unaligned collisions involving unprepared D_2 molecules present in the molecular beam in the $j = 1$ and $j = 2$ rotational levels of $v = 0$. The relative contributions of these process are illustrated in Fig. 10 which shows strong resonance features in the 1-4 K regime[49]. A partial-wave decomposition of these resonances revealed that the dominant contribution is from $L = 4$. Figure 11 compares angular distributions considering both $v = 2$ and $v = 0$ quenchers for H-SARP and V-SARP preparations with the experimental results of Zhou et al[36]. A partial-wave analysis by Zhou et al.[36] through fitting the experimental data to possible outgoing partial waves has suggested that the angular distributions are dominated by a $L = 2$ partial wave resonance. Clearly, this is not supported by theory. We note that experiments do not have energy resolution and includes contributions from a fairly broad range of collision energies centered around 1 K. As illustrated in Fig. 11 the strong forward and backward scattering peaks in the

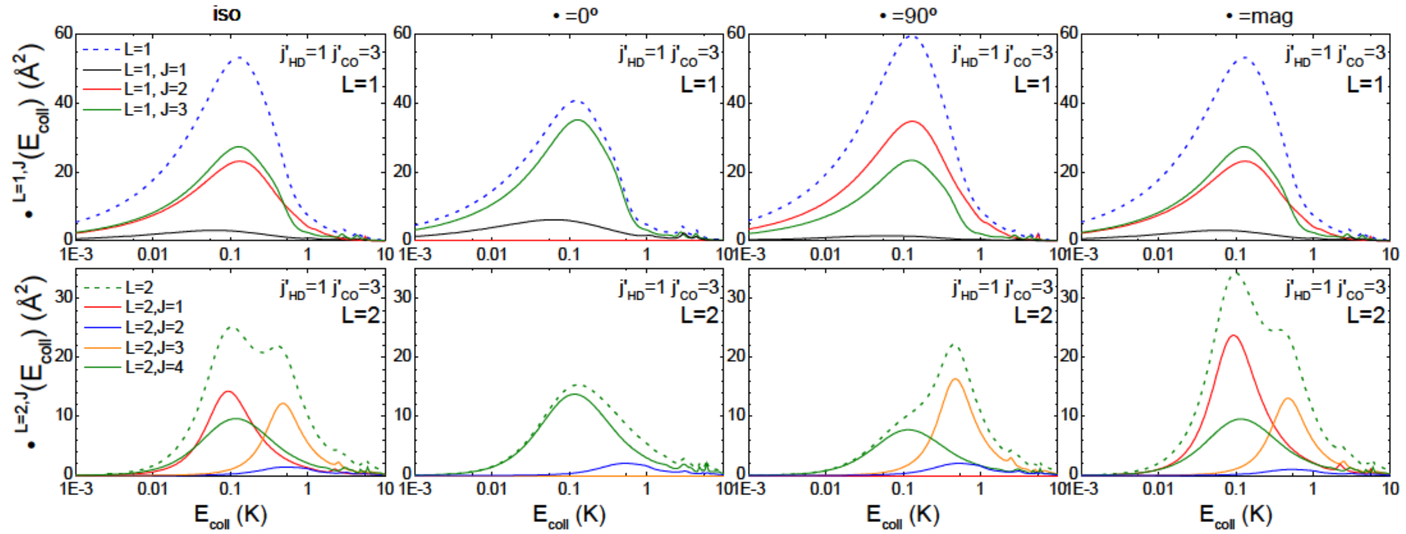

Fig. 9 Partial wave-resolved cross sections for HD($v_1 = 0, j_1 = 2$)+CO($v_2 = 0, j_2 = 0$) → HD($v_1' = 0, j_1'$)+CO($v_2' = 0, j_2'$) collisions for $L = 1$ (upper panel) and $L = 2$ (lower panel) partial waves for the HD($j_1' = 1$) and CO($j_2' = 3$) final states. Note that final rotational levels are labeled as j_{HD}' and j_{CO}' in the figure. Reproduced with permission from[46], 2021, Royal Society of Chemistry.

H-SARP DCS arise from aligned-aligned collisions of the $v = 2$ molecules. The unaligned $v = 0$ quenchers primarily contribute to the background cross sections.

5 Atom-diatom inelastic collisions

Mukherjee, Zare and coworkers have also reported a series of measurements of rotational quenching of HD and D_2 by He[30–35] and D_2 by Ne[34]. These measurements provide $\boldsymbol{k}$-$\boldsymbol{j}$-$\boldsymbol{k'}$ three-vector correlations. The availability of highly accurate interaction potentials for He-H_2[90,91] permits the explicit comparison between theory and experiment. The He-H_2 and He-HD systems have been the topics of extensive quantum coupled-channel calculations of rotational and vibrational transitions due to their importance in astrophysics[92–94]. These studies carried out on different He-H_2 interaction potentials have shown the presence of a strong $L = 1$ partial wave resonance centered around a collision energy of 0.2 cm^{-1} for rotational quenching of HD by He. This is illustrated for both $\Delta j = -1$ and $\Delta j = -2$ transitions in He+HD($v = 1, j = 2$) collisions in Fig. 12[42,43]. Both resonances are very stable among different He-H_2 interaction potentials as illustrated by Morita and Balakrishnan[42,43]. A very weak feature arising from the $L = 2$ partial wave is also present but at a collision energy of about 2.0 cm^{-1}. Figure 13 shows a comparison between experimentally derived DCS[30] for H-SARP, X-SARP and V-SARP preparations of the HD($v = 1, j = 2$) molecule against the theoretical result of Morita and Balakrishnan[42]. It is seen that experiment and theory agree well except for the V-SARP case for which experimental data feature a strong peak near $\theta = 90°$ while theoretical results depict a more isotropic distribution. A partial wave analysis by fitting the experimental angular distributions to outgoing scattering amplitudes has suggested the presence of a strong $L = 2$ partial wave resonance near 1 K[30] but is not supported by theory[42]. This remains a topic of continuing discussions as subsequent experimental studies of $\Delta j = -2$ rotational quenching of HD($v = 2, j = 2$) and D_2($v = 2, j = 2$) by He

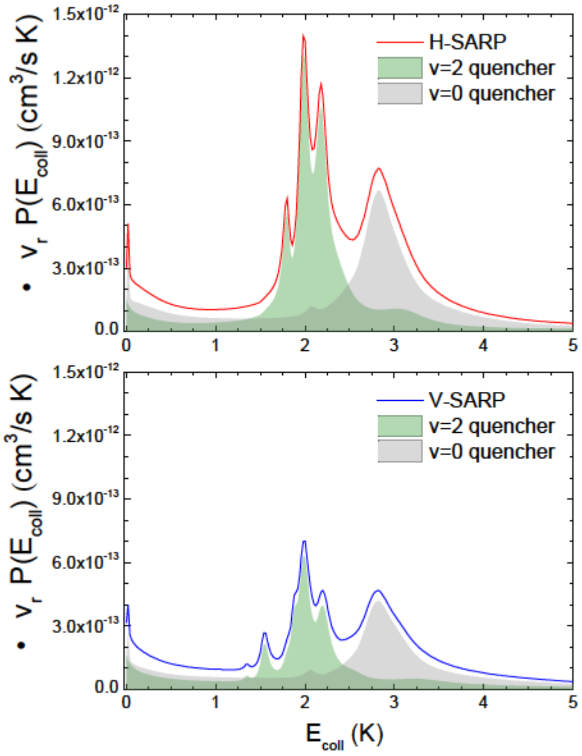

Fig. 10 ICS vs collision energy for rotational quenching of D_2($v = 2, j = 2$) by collisions with D_2($v = 2, j = 2$), D_2($v = 0, j = 1$), and D_2($v = 0, j = 2$). Upper panel: H-SARP preparation; lower panel: V-SARP preparation. For both cases $v = 2$ and $v = 0$ quenchers exhibit different resonance profiles. Reproduced with permission from[49], 2023, American Physical Society.

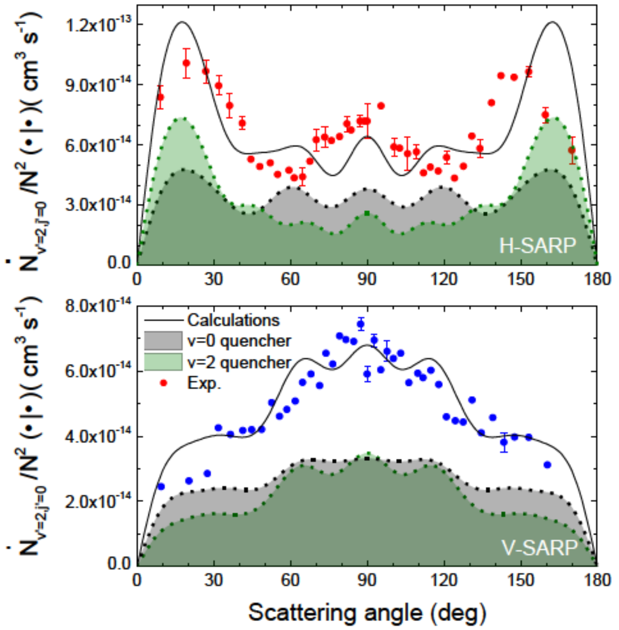

Fig. 11 Angular distributions for rotational quenching of $D_2(v=2, j=2)$ by collisions with $D_2(v=2, j=2)$, $D_2(v=0, j=1)$, and $D_2(v=0, j=2)$ for H-SARP (top) and V-SARP (bottom) preparations compared against experimental data of Zhou et al[36]. The strong forward and backward scattering peaks in H-SARP DCS are attributed to aligned-aligned collisions involving the $v=2$ molecules. Reproduced with permission from[49], 2023 American Physical Society.

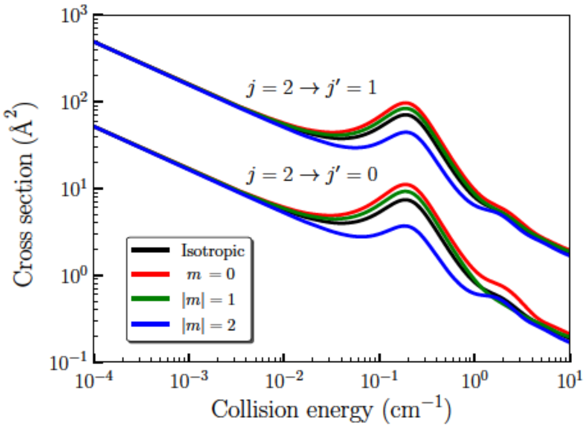

Fig. 12 Integral cross sections for $\Delta j=-1$ and $\Delta j=-2$ rotational quenching of HD($v=1, j=2$) by He as a function of the collision energy for isotropic collisions. Reproduced with permission from[43], 2020, American Institute of Physics.

have also suggested dominant contributions from a $L=2$ resonance[32,33,35]. That such a disagreement exists for simple systems such as He-HD and He-D_2 has raised the possibility of inaccuracies in the He-H_2 potential surface[32,35]. However, the $L=1$ resonance persists when the He-H_2 interaction potentials[90,91] are modified within the uncertainties of the ab initio calculations[42].

Indeed, in a recent SARP experiment on rotational quenching of HD($v=2, j=2$) by He that measured both $\Delta j=-1$ and $\Delta j=-2$ transitions indicated the presence of a strong $L=1$ resonance in the angular distributions for the $\Delta j=-1$ transition[35]. The measured angular distribution for $\Delta j=-1$ could not be fit considering only odd outgoing partial waves which would require the presence of even incoming partial waves and possibly feature a $L=2$ resonance. This finding is in agreement with the cross sections depicted for the $\Delta j=-1$ transition for HD($v=1, j=2$)+He collisions in Fig. 12 that show a strong $L=1$ resonance near 0.2 cm^{-1}[42]. Though this result is for HD($v=1$) our calculations (unpublished) show that for pure rotational transitions in HD by He, the resonance features are not influenced by the initial vibrational state, at least for $v=0-4$ of HD. For $\Delta j=-2$ transitions in HD($v=2, j=2$)+He collisions experiment still attributes key features of the DCS to a $L=2$ resonance which is not supported by theory as in the $v=1$ case discussed above.

Zhou et al. have most recently reported angular distributions for rotational quenching in He+D_2($v=2, j=2$) collisions for H-SARP, X-SARP, and V-SARP preparations[32,33]. Here too, the angular distributions were attributed to a $L=2$ resonance near 1 K while theoretical results of Jambrina et al.[48] show dominant contribution from $L=1$ as in He+HD. As illustrated in Fig. 14 For He+D_2, the $L=1$ resonance is pushed to an order of magnitude lower in energy, occurring near 0.02 K but with a magnitude that is two orders greater than that of He+HD[48]. Though the $L=1$ resonance occurs in the tail of the experimental velocity distribution due to its large magnitude it still dominates the velocity averaged DCS as illustrated by Jambrina et al[48]. As a result, theoretical DCS averaged over the experimental velocity distribution show signatures of the $L=1$ resonace and do not agree with the measurements. However, if the $L=1$ resonance is artificially suppressed by omitting contributions from collision energies below 1 K in the velocity average, theoretically predicted DCS agrees with experiment as illustrated in Fig. 15[48]. Given the fact that theory agrees with experiment when the $L=1$ resonance contribution is artificially removed, it is possible that $L=1$ collisions may not be accessed in the experiments. The robustness of the $L=1$ resonance is topic of an ongoing study in our group and will be addressed in an upcoming publication.

The biaxial X-SARP preparation corresponds to a linear superposition of $m=\pm1$ states. Zhou et al. have shown that, for j=2, this state can also be expressed as a linear combination of two uniaxial states that correspond to simultaneous alignments of $\beta=\pm45°$. For details we refer to Zhou et al.[33] and Jambrina et al[48]. For this case, the angular distribution integrated over the azimuthal angle still retains an interference term that is unique for the bi-axial preparation.

Stereodynamic effects in rotational quenching of HF($j=1,2$) by collisions with H at collision energies from 10^{-3}-100 K have recently been reported by Jambrina et al.[41,45]. For both $j=1\to0$ and $j=2\to1$ transitions quasibound states corresponding to a $L=3$ partial wave appear as a shape resonance near 5 K that dominates the cross section in the 1-10 K regime. While several total angular momentum quantum numbers $J=0-5$ contribute in this regime, partial wave contribution from $L=3$ is found to dominate for the two initial rotational levels as shown in Fig. 16[45]. Strong stereodynamic effects are also observed in this sys-

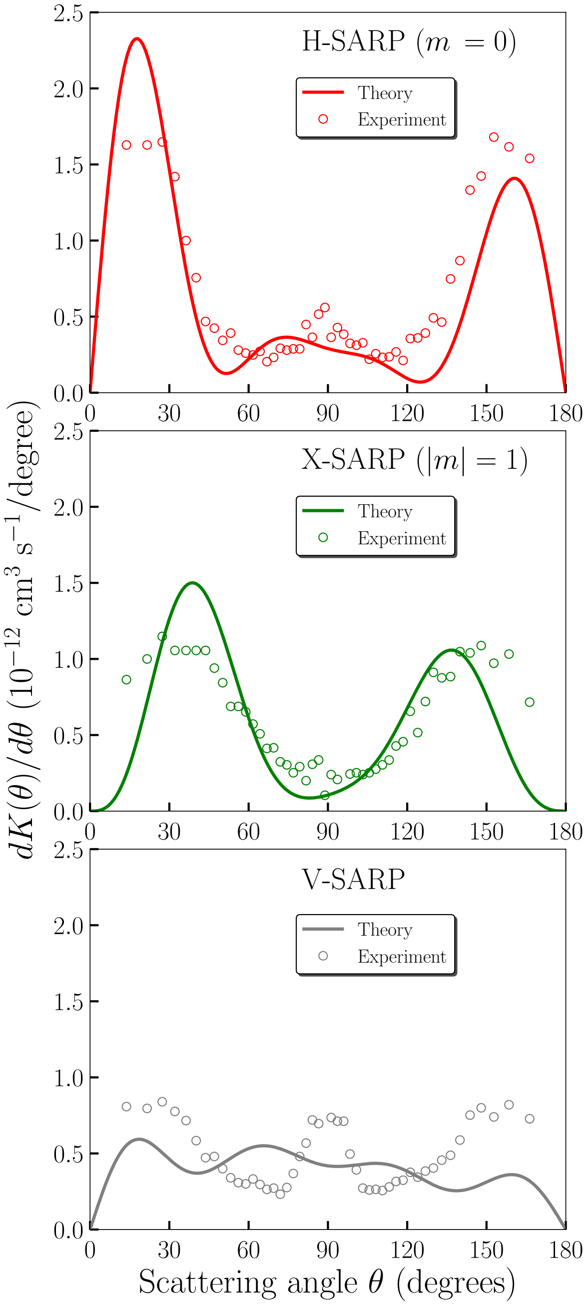

Fig. 13 Angular distributions for $j \quad 2$ rotational quenching of HD($v \quad 1 \; j \quad 2$) by He for H-SARP, X-SARP, and V-SARP preparations. The theoretical angular distributions have not been symmetrized. Reproduced with permission from [42], 2020, American Institute of Physics.

tem, in particular, in the resonance region as Fig. 17 illustrates[45]. The 0 preparation enhances the cross sections and rate coefficients while 90 alignment suppresses both. This suppression is most striking in the region of the $L \quad 3$ resonance.

6 Atom-diatom reactive scattering

Experiments on inelastic collisions of SARP prepared molecules have largely focused on pure rotational quenching in cold collisions. Reactive collisions have mostly been explored only theoretically. One exception is the recent crossed beam experimental study of the H+HD($v \quad 1 \; j \quad 2$) H_2+D chemical reaction by Wang et al.[95] at collision energies of 0.5, 1.2, and 2.07 eV. The HD molecules were prepared in H-SARP and V-SARP alignments and the corresponding DCSs display strong stereodynamic effect as illustrated in Fig. 18[95]. Accompanying quantum scattering calculations revealed strong constructive interference for the V-SARP alignment leading to distinct angular distributions compared to the H-SARP case. The interference effect leads to a strong enhancement of side-ways scattering that is predominant for the V-SARP case. In these experiments angular distributions are not integrated over the azimuthal angle (or) but correspond to 0 (in-plane scattering). As discussed in Section 4, integration over the azimuthal angle washes out the interference term arising from different m_j states in the V-SARP preparation.

In a recent theoretical study, da Silva Jr. et al.[96] reported pronounced stereodynamical effects in the H+D_2 v 4 j D+HD($v \quad j$) reaction and its reverse process at collision energies between 1-50 K. Because the H+D_2 $v \quad 0$ HD+H reaction has an energy barrier exceeding 0.3 eV and the reaction is endoergic at low temperatures (due to the difference in zero-point energies of D_2 and HD) the reaction does not occur at low temperatures. In previous studies it has been shown that the vibrationally adiabatic barrier decreases with vibrational excitation of D_2 and HD, and for $v \quad 3$ and higher, the reaction occurs along a barrierless pathway even at ultracold temperatures[97–99]. Figure 19 shows the DCS, integrated over the azimuthal angle, as a function of the scattering angle for the H+D_2 $v \quad 4 \; j \quad 2$ HD(v 3 $j \quad 0$) reaction for collision energies of 1 K, 5 K, and 10 K and for different alignment angles 0 15 45 60 75 , and 90 [96]. It is seen that the angular distribution becomes progressively backward scattered as the collision energy increases from 1 K to 10 K. Strong stereodynamic effects are observed at all collision energies with 0 (H-SARP) leading to enhancement and 90 (V-SARP) leading to almost complete suppression of the reaction. Stereodynamics at higher collision energies for the D+H_2 HD+H was also investigated by Aldegunde et al.,[57] and more recently for the H+D_2 $v \quad 0 \; j \quad 2$ HD $v \quad j$ +D reaction by Jambrina et al. [87] where the effects were analyzed in terms of GDFs as shown in Fig. 1. In both cases, strong alignment effects in the angular distribution of the scattered HD molecule were found.

Stereodynamic effects in F+HD $v \quad 0 \; 1 \; j \quad 1$ HF+D; DF+H reactions were recently reported by Sáez-Rábanos et al[47]. As illustrated in Fig. 20 , for both HF+D and DF+H channels, two resonance peaks corresponding to the $L \quad 3$ partial wave dominates the ICS at energies of 0.05 meV (0.6 K) and 0.6 meV (

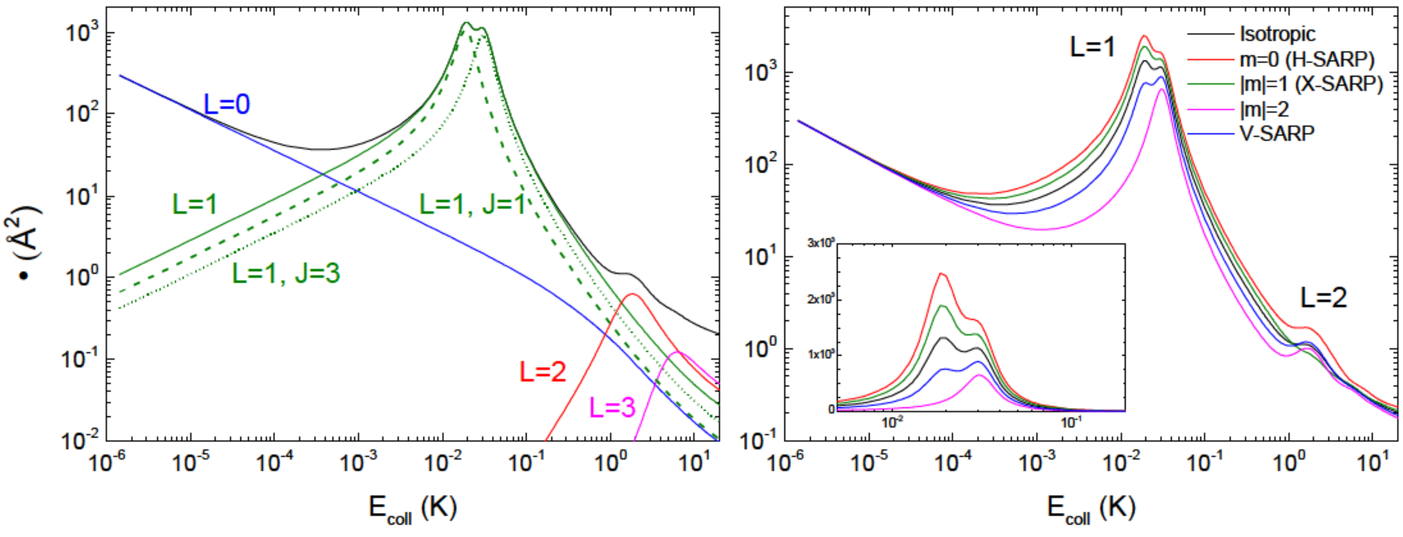

Fig. 14 Partial-wave resolved Integral cross sections for rotational quenching of $D_2(v=2, j=2)$ by He for isotropic collisions (left panel). ICS for different SARP preparations (right panel) are compared against isotropic collisions. Reproduced with permission from [48], 2022, American Chemical Society.

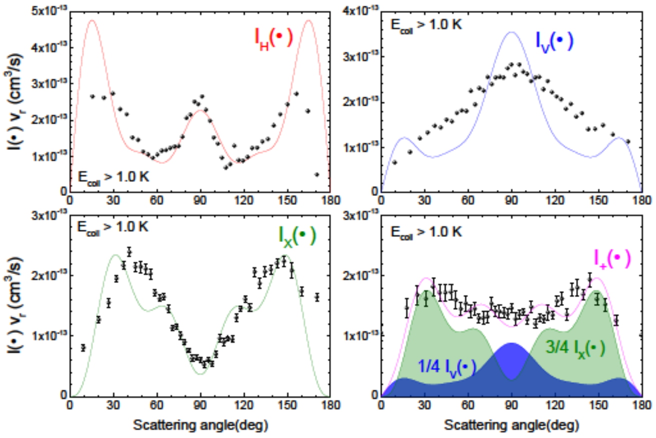

Fig. 15 Velocity-averaged differential rate coefficients for D_2 $(v=2, j=2 \rightarrow v'=2, j'=0)$ by collisions with He for the H-SARP, V-SARP, X-SARP, and 45-SARP preparations of the initial D_2 orientations as functions of the scattering angle. Results are shown excluding Ecoll < 1 K. Reproduced with permission from [48], 2022, American Chemical Society.

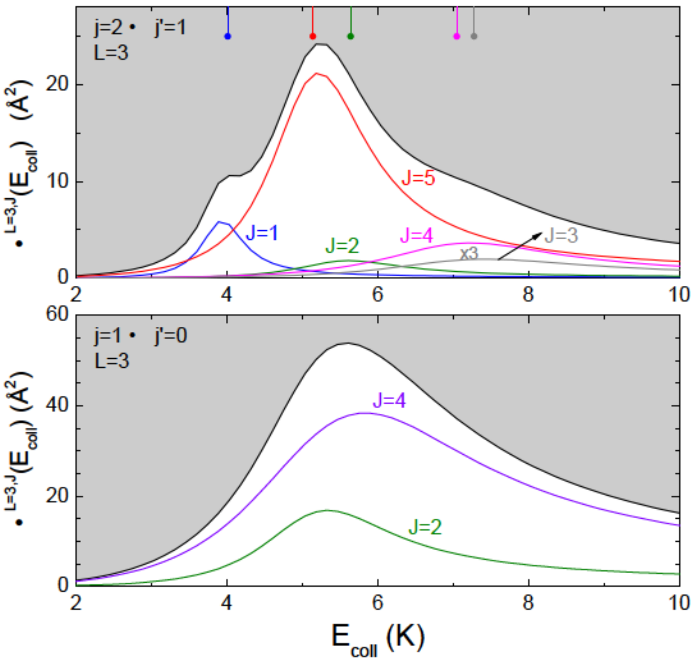

Fig. 16 Partial-wave resolved ICSs for rotational quenching of HF$(j=1,2)$ by H as functions of the collision energy for different values of the total angular momentum quantum number J. Upper panel: $j=2 \rightarrow j'=1$; Lower panel: $j=1 \rightarrow j'=0$. Reproduced with permission from [41], 2019, Royal Society of Chemistry.

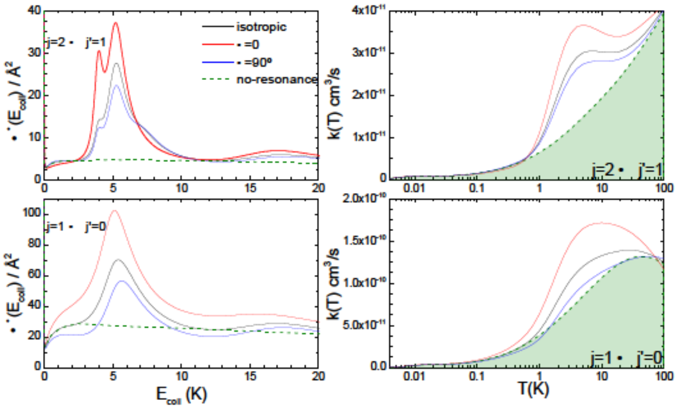

Fig. 17 Left panel: Alignment dependent ICSs for rotational quenching of HF($j=1,2$) by collisions with H as functions of the collision energy. The background cross section when the resonance contribution is removed is shown by the dashed curve; right panel: corresponding thermal rate coefficients that show strong enhancement from the $L=3$ resonance for $T=1-20$ K. Reproduced with permission from [41], 2019, Royal Society of Chemistry.

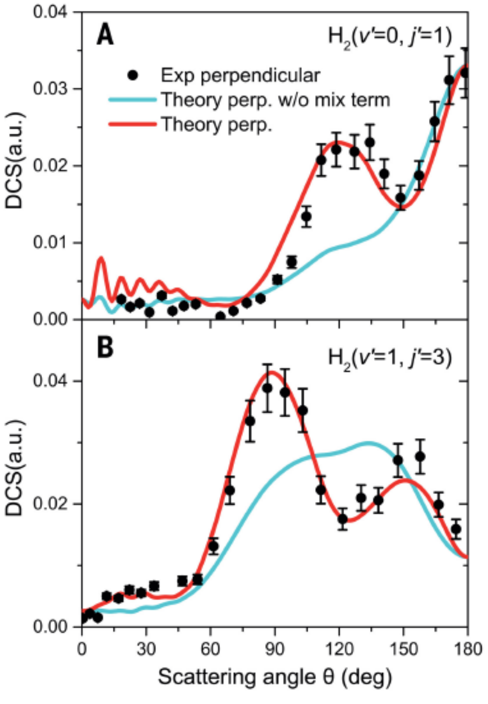

Fig. 18 Comparisons between experimental and theoretical DCSs for reactive H+HD($v=1, j=2$)→D+H$_2$ collisions for V-SARP preparations of the HD molecule. Note that if the interference term is suppressed in the theory no agreement is found with experiment. Reproduced with permission from [95], 2023, American Association for the Advancement of Science.

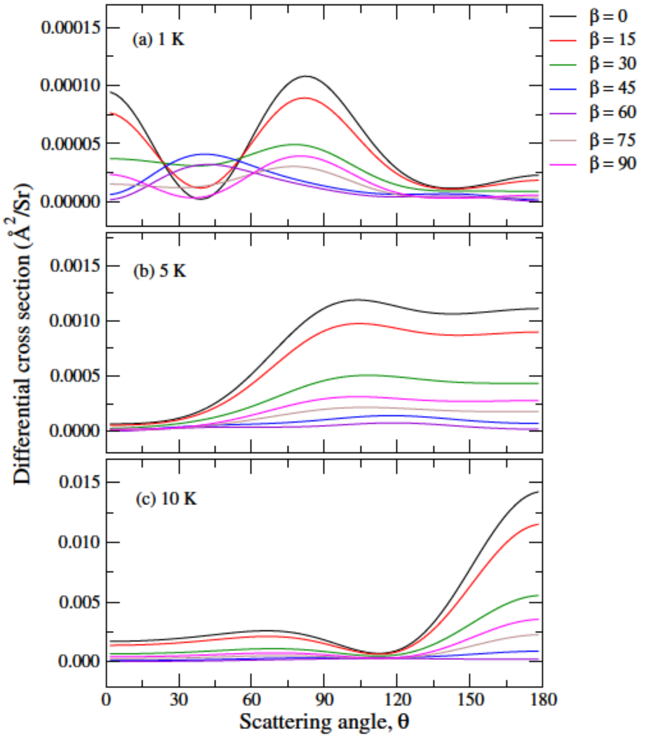

Fig. 19 Angular distributions for the H+D$_2$($v=4, j=2$) →HD($v=3, j=0$)+D reaction, integrated over the azimuthal angle, as a function of the scattering angle for different alignment angle β. Reproduced with permission from [96], 2022, American Institute of Physics.

7.0 K) with the former being the dominant feature. The intensity of the resonances for $v=1$ was found to be an order of magnitude greater than that of $v=0$. For the latter, stereodynamic effects were found to be marginal for the dominant HF channel while strong suppression of the resonance at 0.05 meV was observed for DF channel for $\beta=0°$. This effect is reversed for the $v=1$ reaction for which $\beta=0°$ alignment enhances the resonance feature at 0.05 meV relative to isotropic scattering as in the case of the H+D$_2$ reaction discussed above.

7 Atom-triatom inelastic collisions

While the vast majority of experimental and theoretical studies of stereodynamic control of inelastic and reactive collisions were targeted at atom-diatom and diatom-diatom collisions, polyatomic molecules are expected to present even richer effects due to their multiple degrees of freedom and the stronger anisotropy of the interaction potential. This is a challenging problem for both experiment and theory. Recently Yang, Xie, and Guo [100] explored this effect for triatomic molecules taking rotationally inelastic collisions in H$_2$O+He as a test case and by treating the H$_2$O molecule as a rigid rotor. Figure 21 shows partial-wave resolved ICS and the ICS for isotropic, V-SARP, and H-SARP preparations for the $1_{0,1^-} \leftarrow 1_{1,0^-}$ rotational transition as a function of the collision energy in K [100]. Note that in this case V-SARP corresponds to a preferential horizontal alignment of the water molecule relative to the incident velocity vector, whereas the H-SARP preparation corresponds to a preferential vertical alignment. The partial-wave resolved cross sections reveal that the strongly peaked resonance at

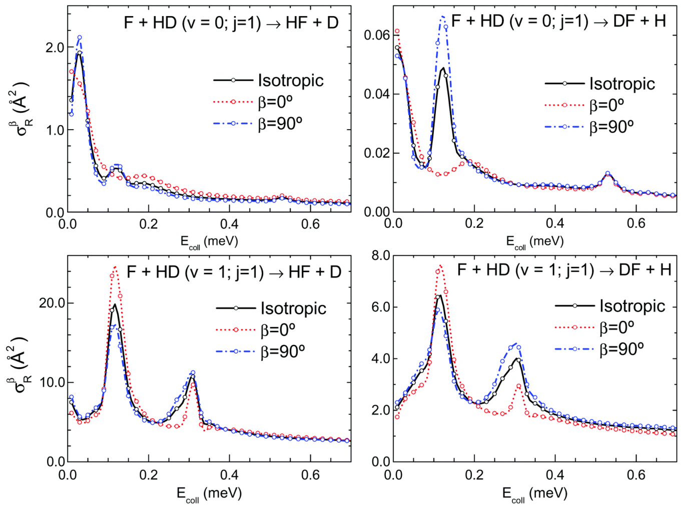

Fig. 20 Alignment-dependent ICSs for the F+HD v 0 1 j 1 HF+D & DF+H reactions as a function of the collision energy in meV. Reproduced with permission from [47], 2021, Royal Society of Chemistry.

2.85 K primarily arises from a L 5 partial wave while the weaker resonance near 8 K corresponds to L 6. The resonance peak at 3.24 K has contributions from both L 3 and L 5. It is seen that while the H-SARP preparation yields results in close agreement with the isotropic case, the V-SARP alignment yields smaller cross sections, except at the dominant resonance near 2.85 K. The differences are amplified in the DCS shown in Fig. 22, including the resonance region depicted in the bottom panel [100] . In particular, for the resonance at 3.24 K, the H-SARP and V-SARP results are out of phase in their oscillatory behavior. Clearly, more theoretical and experimental studies are needed to unravel the complex stereodynamic effects expected for polyatomic molecules.

8 Outlook and future prospects

It has long been known that stereodynamics is an important aspect of chemical reactions and inelastic collisions. There is a long history of probing the effect of reactant polarization on the product quantum state populations. The stereodynamics of inelastic collisions with open-shell molecules has been widely explored, especially for collisions involving OH or NO in which the internuclear axis was oriented using hexapole and orienting fields, leading to the measurement of the integral steric asymmetry. [101–106] More recently, a major breakthrough was achieved with the measurements of state-to-state differential cross section for oriented NO molecules with rare gases, [58,60,107–111] allowing the determination of both differential and integral steric effects. It was shown that by changing the direction of the orienting field with respect to the relative velocity, a remarkable control could be exerted over the branching between the spin-orbit changing and the spin-orbit conserving rotational product channels. In another recent experiment, direct measurement of the four-vector correlation between initial and final relative velocities and rotational angular momenta in collisions of electronically excited NO(A) and Ne has been reported [112]. In particular, non-intuitive changes in the orientation from reactants to products for specific states and scatter-

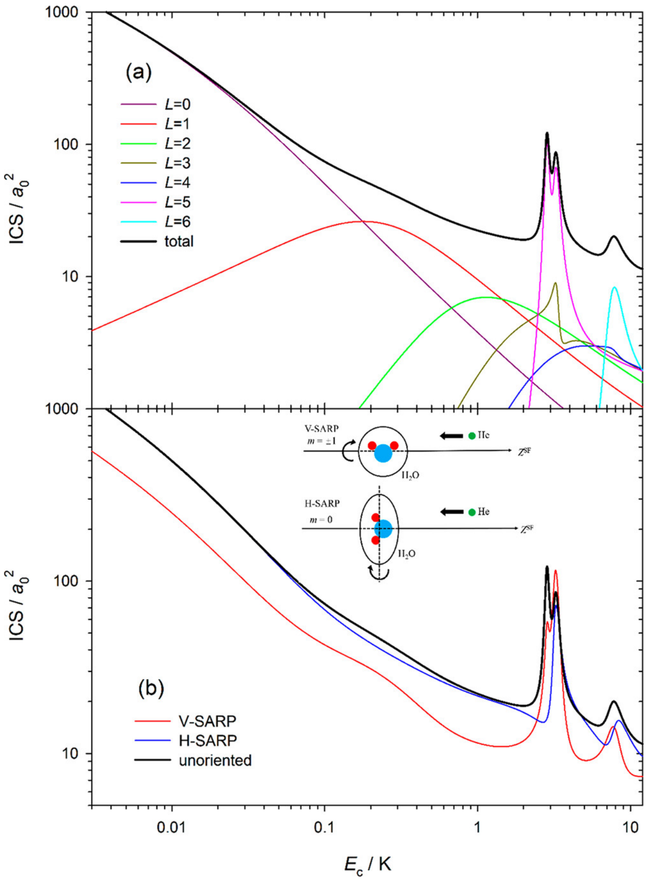

Fig. 21 Upper panel: Partial wave resolved ICS for V-SARP, H-SARP, and isotropic collisions as a function of the collision energy in K for the $1_{0\,1}$ 1_{10} rotational transition in H_2O induced by He; Lower panel: ICS for the same transition for 0 different initial SARP preparations of the H_2O molecule. Reproduced with permission from [100], 2022, American Chemical Society.

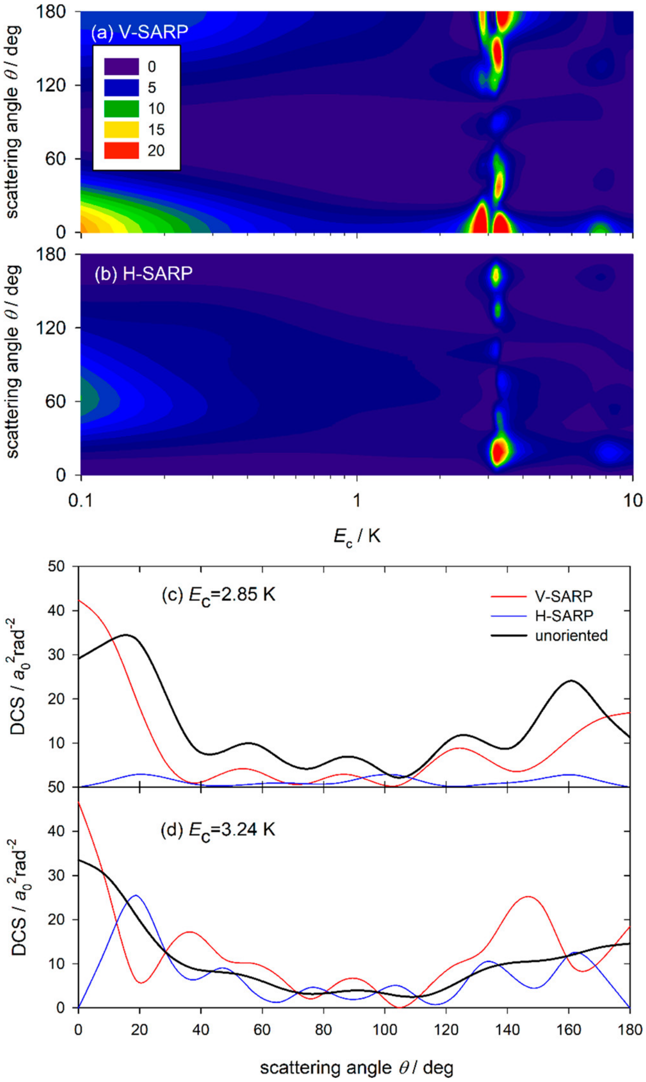

Fig. 22 Upper panels (a) and (b): DCS as a function of the collision energy for V-SARP and H-SARP preparations for the $1_{0 1}$ $1_{1 0}{}^{1}$ rotational transition in H_2O induced by He; Lower panels (c) and (d): DCS corresponding to the resonance peaks at 2.85 K and 3.24 K in the ICS depicted in Fig. 21. Reproduced with permission from[100], 2022, American Chemical Society.

ing angles were observed[112]. In all these cases, the experimental result could be reproduced by quantum scattering calculations almost perfectly.

The stereodynamics of reactive collisions has also received considerable attention. As an example, it has been found that stereodynamics seems to explain the preference for given -doublet of the OD radical that was experimentally found in the $O(^3P)+D_2$ reaction.[113–115] The stereodynamics of polyatomic reactions has also been subject of experimental investigations. In particular, Liu and coworkers have carried out extensive studies using a crossed molecular beam, product imaging approach on the effects of the CH_3-stretching excitations of $CH_3D(v_1$ $1)$ in reactions with the Cl-atom[116–120]. By active control of the polarization direction of an IR laser under chosen beam-geometries, a complete set of polarization-dependent differential cross sections is disentangled from the ion image of the methyl product. The results provide a complete description of the most detailed stereo-requirement that can be achieved for a reaction. Although these studies were carried out at thermal or hyperthermal collision energies, it can be expected that similar experimental investigations can be performed in the cold energy regime by making use of merging beams.

The studies just referred to above were carried out with polar molecules and their experimental setups are not suitable to study collisions of non-polar molecules. The introduction of the SARP techniques allows preferential alignments of the molecular bond axis relative to the initial velocity vector and make it possible to study stereodynamical effects in rotationally inelastic and reactive collisions with H_2 and its isotopic variants. So far, except the reactive scattering in H+HD collisions that employed a crossed-molecular beam setup[95], the experimental studies of rotationally inelastic collisions by Perreault et al. and Zhou et al. used co-expansion of the two colliding species in the same molecular beam. This leads to a fairly broad range of collision energies and the measured angular distribution involves an average (integration) over these collision energies. Thus, unless the scattering is dominated by a single partial wave, the angular distribution reflects contributions from all allowed incoming partial waves. This can smear the effect of any resonances present in the energy-dependent cross sections. Clearly, theoretical calculations are needed to unveil these resonance features and the results on $HD+H_2$, D_2+D_2, HD+He and D_2+He have illustrated the presence of shape resonances arising from low angular momentum partial waves. Because the scattering is dominated by a few partial waves in these systems (mostly L 0 4) for collision energies near 1 K, markedly pronounced control over the collision outcome is possible, making stereodynamical preparation as an important tool in controlling the collision outcome.

One approach to explicitly detect scattering resonances in SARP experiments would be to employ pre-cooled reactants so that their relative velocity distribution would be narrower. This could be combined with the merged beam techniques in which collision energy can be varied by several orders of magnitude by varying the merging angle. Narrow resonances in energy-resolved cross sections from such measurements were demonstrated for Penning ionization of H_2 by He by Narevicius and coworkers[121–123].

We expect such techniques would be extended to SARP prepared molecules in the near future.

So far, the experimental results of rotational transitions reported by Perreault et al. and Zhou et al. do not provide the azimuthal angle ( ) resolution of the differential cross sections. This makes any interference term arising from the different m_j components of the initial rotational level j to be unobservable. The reactive scattering study of the H+HD collisions by Wang et al.[95] that does not include integration over the azimuthal angle (a choice of 0 is made in the initial preparation) has shown pronounced interference effects in the V-SARP preparation of the HD molecule. The experiment corresponds to high collision energies and such interference effects are expected to be even more significant in cold collisions. One approach to extend these studies to lower temperatures would be to vibrationally excite the HD molecules to v 3 or higher for which the reaction becomes essentially barrierless. The SARP techniques can be extended to coherent control of molecular collisions where interference effects are expected to dominate the collision outcome. Indeed, such interference effects have been theoretically demonstrated by Devolder, Tscherbul and Brumer for reactive scattering in F+H_2/HD collisions and spin-relaxation in O_2+O_2 collisions[124,125]. Control of reactive collisions in KRb+KRb collisions using a rudimentary model has also been explored by Devolder et al.[126]. In these theoretical studies reactant molecules are prepared in a coherent superposition of m_j or spin states. We believe, this would be a next frontier in cold collisions where quantum effects are significantly amplified through coherent control and stereodynamic preparations. Non-adiabatic effects in cold and ultracold chemical reactions have also received much attention recently[24,127,128] and how stereodynamical preparation influences reactivity in these systems remains an open question. As commented on above, collisions of more complex molecules than diatomics have been experimentally probed, but nevertheless stereodynamics of polyatomic molecules remains largely unexplored where anisotropic interactions are expected to dominate.

The stereodynamics approach discussed here is one avenue for controlling molecular collisions that can be applied to cold as well as hot collisions though the control is expected to be more dramatic for collisions dominated by a few partial waves as illustrated in this article. For ultracold collisions of dipolar molecules it has been demonstrated that strong control over the collision outcome can be achieved through an applied electric field or confining collisions to reduced dimensions[129–131]. Controlling ultracold collisions through applied electric, magnetic, and microwave fields is rapidly emerging as an important topic in ultracold chemistry[132–134]. Clearly, the outlook appears to be very bright for quantum control of molecular collisions and chemical reactions.

Author Contributions

All authors contributed to manuscript preparation and editing.

Conflicts of interest

There are no conflicts to declare.

Acknowledgements

This work is supported in part by NSF grant No. PHY-2110227 (N.B.) and by a MURI grant from Army Office of Research (Grant No. W911NF-19-1-0283 to H.G. and N.B.). F.J.A. acknowledges funding by the Spanish Ministry of Science and Innovation (grant PID2021-122839NB-I00). P.G.J. acknowledges Grant No. PID2020-113147GA-I00 funded by MCIN/AEI/10.13039/501100011033 (Spanish Ministry of Science and Innovation).

Notes and references

1 L. D. Carr, D. DeMille, R. V. Krems and J. Ye, *New J. Phys.*, 2009, **11**, 055049.
2 R. V. Krems, *Molecules in Electromagnetic Fields*, John Wiley & Sons, Ltd, 2018.
3 N. Balakrishnan, *J. Chem. Phys.*, 2016, **145**, 150901.
4 J. L. Bohn, A. M. Rey and J. Ye, *Science*, 2017, **357**, 1002–1010.
5 J. Toscano, H. J. Lewandowski and B. R. Heazlewood, *Phys. Chem. Chem. Phys.*, 2020, **22**, 9180–9194.
6 M.-G. Hu, Y. Liu, D. D. Grimes, Y.-W. Lin, A. H. Gheorghe, R. Vexiau, N. Bouloufa-Maafa, O. Dulieu, T. Rosenband and K.-K. Ni, *Science*, 2019, **366**, 1111–1115.
7 Y. Liu, M.-G. Hu, M. A. Nichols, D. D. Grimes, T. Karman, H. Guo and K.-K. Ni, *Nat. Phys.*, 2020.
8 Y. Liu and K.-K. Ni, *Annu. Rev. Phys. Chem.*, 2022, **73**, 73–96.
9 R. Wynar, R. S. Freeland, D. J. Han, C. Ryu and D. J. Heinzen, *Science*, 2000, **287**, 1016.
10 S. Inouye, J. Goldwin, M. L. Olsen, C. Ticknor, J. L. Bohn and D. S. Jin, *Phys. Rev. Lett.*, 2004, **93**, 183201.
11 C. Chin, R. Grimm, P. Julienne and E. Tiesinga, *Rev. Mod. Phys.*, 2010, **82**, 1225.
12 J. D. Weinstein, R. de Carvalho, T. G. B. Friedrich and J. M. Doyle, *Nature*, 1998, **395**, 148.
13 J. Doyle, B. Friedrich, R. Krems and F. Masnou-Seeuws, *Eur. Phys. J. D*, 2004, **31**, 149–164.
14 N. R. Hutzler, H.-I. Lu and J. M. Doyle, *Chem. Rev.*, 2012, **112**, 4803.
15 H. L. Bethlem, G. Berden and G. Meijer, *Phys. Rev. Lett.*, 1999, **83**, 1558.
16 H. L. Bethlem and G. Meijer, *Int. Rev. Phys. Chem.*, 2003, **22**, 73.
17 S. Y. T. van de Meerakker, H. L. Bethlem, N. Vanhaecke and G. Meijer, *Chem. Rev.*, 2012, **112**, 4828.
18 E. S. Shuman, J. F. Barry and D. DeMille, *Nature*, 2010, **467**, 820.
19 J. M. Sage, S. Sainis, T. Bergeman and D. DeMille, *Phys. Rev. Lett.*, 2005, **94**, 203001.
20 S. Ospelkaus, K.-K. Ni, D. Wang, M. H. G. de Miranda, B. Neyenhuis, G. Quéméner, P. S. Julienne, J. L. Bohn, D. S. Jin and J. Ye, *Science*, 2010, **327**, 853–857.
21 J. F. E. Croft, C. Makrides, M. Li, A. Petrov, B. K. Kendrick, N. Balakrishnan and S. Kotochigova, *Nat. Commun*, 2017, **8**, 15897.

22 J. F. E. Croft, N. Balakrishnan and B. K. Kendrick, *Phys. Rev. A*, 2017, **96**, 062707.

23 B. K. Kendrick, *J. Chem. Phys.*, 2021, **154**, 124303.

24 B. K. Kendrick, H. Li, M. Li, S. Kotochigova, J. F. E. Croft and N. Balakrishnan, *Phys. Chem. Chem. Phys.*, 2021, **23**, 5096–5112.

25 N. Mukherjee and R. N. Zare, *J. Chem. Phys.*, 2011, **135**, 024201.

26 N. Mukherjee, W. E. Perreault and R. N. Zare, *J. Phys. B*, 2017, **50**, 144005.

27 W. E. Perreault, N. Mukherjee and R. N. Zare, *J. Chem. Phys.*, 2016, **145**, 154203.

28 W. E. Perreault, N. Mukherjee and R. N. Zare, *Science*, 2017, **358**, 356–359.

29 W. E. Perreault, N. Mukherjee and R. N. Zare, *Nature Chem*, 2018, **10**, 561–567.

30 W. E. Perreault, N. Mukherjee and R. N. Zare, *J. Chem. Phys.*, 2019, **150**, 174301.

31 W. E. Perreault, H. Zhou, N. Mukherjee and R. N. Zare, *Phys. Rev. Lett.*, 2020, **124**, 163202.

32 H. Zhou, W. E. Perreault, N. Mukherjee and R. N. Zare, *J. Chem. Phys.*, 2021, **154**, 104309.

33 H. Zhou, W. E. Perreault, N. Mukherjee and R. N. Zare, *Science*, 2021, **374**, 960–964.

34 W. E. Perreault, H. Zhou, N. Mukherjee and R. N. Zare, *J. Chem. Phys.*, 2022, **157**, 144301.

35 W. E. Perreault, H. Zhou, N. Mukherjee and R. N. Zare, *J. Phys. Chem. Lett.*, 2022, **13**, 10912–10917.

36 H. Zhou, W. E. Perreault, N. Mukherjee and R. N. Zare, *Nat. Chem.*, 2022, **14**, 658–663.

37 N. Mukherjee, *J. Phys. Chem. Lett.*, 2023, **127**, 418–438.

38 J. F. E. Croft, N. Balakrishnan, M. Huang and H. Guo, *Phys. Rev. Lett.*, 2018, **121**, 113401.

39 J. F. E. Croft and N. Balakrishnan, *J. Chem. Phys.*, 2019, **150**, 164302.

40 P. G. Jambrina, J. F. E. Croft, H. Guo, M. Brouard, N. Balakrishnan and F. J. Aoiz, *Phys. Rev. Lett.*, 2019, **123**, 043401.

41 P. G. Jambrina, L. González-Sánchez, J. Aldegunde, V. Sáez-Rábanos and F. J. Aoiz, *J. Phys. Chem. A*, 2019, **123**, 9079–9088.

42 M. Morita, Q. Yao, C. Xie, H. Guo and N. Balakrishnan, *Phys. Rev. Research*, 2020, **2**, 032018.

43 M. Morita and N. Balakrishnan, *J. Chem. Phys.*, 2020, **153**, 091101.

44 M. Morita and N. Balakrishnan, *J. Chem. Phys.*, 2020, **153**, 184307.

45 P. G. Jambrina, L. González-Sánchez, M. Lara, M. Menéndez and F. J. Aoiz, *Phys. Chem. Chem. Phys.*, 2020, **22**, 24943–24950.

46 P. G. Jambrina, J. F. E. Croft, N. Balakrishnan and F. J. Aoiz, *Phys. Chem. Chem. Phys.*, 2021, **23**, 19364–19374.

47 V. Sáez-Rábanos, J. E. Verdasco, F. J. Aoiz and V. J. Herrero, *Phys. Chem. Chem. Phys.*, 2021, **23**, 8002–8012.

48 P. G. Jambrina, M. Morita, J. F. E. Croft, F. J. Aoiz and N. Balakrishnan, *J. Phys. Chem. Lett.*, 2022, **13**, 4064–4072.

49 P. G. Jambrina, J. F. E. Croft, J. Zuo, H. Guo, N. Balakrishnan and F. J. Aoiz, *Phys. Rev. Lett.*, 2023, **130**, 033002.

50 D. Case and D. Herschbach, *Mol. Phys.*, 1975, **30**, 1537–1564.

51 D. A. Case and D. R. Herschbach, *J. Chem. Phys.*, 2008, **64**, 4212–4222.

52 R. B. Bernstein, D. R. Herschbach and R. D. Levine, *J. Phys. Chem.*, 1987, **91**, 5365–5377.

53 M. H. Alexander, P. J. Dagdigian and A. E. DePristo, *J. Chem. Phys.*, 1977, **66**, 59–66.

54 A. J. Orr-Ewing and R. N. Zare, *Annu. Rev. Phys. Chem.*, 1994, **45**, 315–366.

55 M. P. de Miranda, F. J. Aoiz, L. Bañares and V. Sáez-Rábanos, *J. Chem. Phys.*, 1999, **111**, 5368–5383.

56 M. P. d. Miranda and F. J. Aoiz, *Phys. Rev. Lett.*, 2004, **93**, 083201.

57 J. Aldegunde, M. P. de Miranda, J. M. Haigh, B. K. Kendrick, V. Sáez-Rábanos and F. J. Aoiz, *J. Phys. Chem. A*, 2005, **109**, 6200–6217.

58 F. J. Aoiz, M. Brouard, S. D. S. Gordon, B. Nichols, S. Stolte and V. Walpole, *Phys. Chem. Chem. Phys.*, 2015, **17**, 30210–30228.

59 F. J. Aoiz and M. P. de Miranda, in *Tutorials in Molecular Reaction Dynamics*, ed. M. Brouard and C. Vallance, RSC Publishing, 2010.

60 C. G. Heid, V. Walpole, M. Brouard, P. G. Jambrina and F. J. Aoiz, *Nat. Chem.*, 2019, **11**, 662–668.

61 J. Aldegunde, P. G. Jambrina, V. Sáez-Rábanos, M. P. de Miranda and F. J. Aoiz, *Chem. Phys. Phys. Chem.*, 2010, **12**, 13626.

62 J. Aldegunde, J. M. Alvariño, M. P. de Miranda, V. Sáez Rábanos and F. J. Aoiz, *J. Chem. Phys.*, 2006, **125**, 133104.

63 J. Aldegunde, P. G. Jambrina, M. P. de Miranda, V. S. Rábanos and F. J. Aoiz, *Phys. Chem. Chem. Phys.*, 2011, **13**, 8345–8358.

64 N. Balakrishnan and A. Dalgarno, *Chem. Phys. Lett.*, 2001, **341**, 652–656.

65 K. K. Ni, S. Ospelkaus, D. Wang, G. Quéméner, B. Neyenhuis, M. H. G. de Miranda, J. L. Bohn, J. Ye and D. S. Jin, *Nature*, 2010, **464**, 1324–1328.

66 Y. Liu, D. D. Grimes, M.-G. Hu and K.-K. Ni, *Phys. Chem. Chem. Phys.*, 2020, **22**, 4861–4874.

67 M.-G. Hu, Y. Liu, M. A. Nichols, L. Zhu, G. Quéméner, O. Dulieu and K.-K. Ni, *Nat. Chem.*, 2021, **13**, 435–440.

68 Y. Liu, M.-G. Hu, M. A. Nichols, D. Yang, D. Xie, H. Guo and K.-K. Ni, *Nature*, 2021, **593**, 379–384.

69 F. H. Mies, *J. Chem. Phys.*, 1984, **80**, 2514–2525.

70 J. P. Burke, C. H. Greene and J. L. Bohn, *Phys. Rev. Lett.*, 1998, **81**, 3355–3358.

71 E. J. Rackham, T. Gonzalez-Lezana and D. E. Manolopoulos, *J. Chem. Phys.*, 2003, **119**, 12895–12907.

72 T. González-Lezana, *Int. Rev. Phys. Chem.*, 2007, **26**, 29–91.
73 D. Yang, J. Huang, X. Hu, D. Xie and H. Guo, *J. Chem. Phys.*, 2020, **152**, 241103.
74 B. Yang, P. C. Stancil, N. Balakrishnan and R. C. Forrey, *J. Chem. Phys.*, 2006, **124**, 104304.
75 D. R. Flower, *Mon. Not. R. Astron. Soc.*, 2012, **425**, 1350–1356.
76 B. Yang, P. Zhang, X. Wang, P. C. Stancil, J. M. Bowman, N. Balakrishnan and R. C. Forrey, *Nat. Commun*, 2015, **6**, 6629.
77 B. Yang, N. Balakrishnan, P. Zhang, X. Wang, J. M. Bowman, R. C. Forrey and P. C. Stancil, *J. Chem. Phys.*, 2016, **145**, 034308.
78 A. Faure, P. Jankowski, T. Stoecklin and K. Szalewicz, *Sci. Rep.*, 2016, **6**, 28449.
79 S. Chefdeville, T. Stoecklin, C. Naulin, P. Jankowski, K. Szalewicz, A. Faure, M. Costes and A. Bergeat, *Astrophys. J. Letters*, 2015, **799**, L9.
80 M. Costes and C. Naulin, *Chem. Sci.*, 2016, **7**, 2462–2469.
81 C. Amarasinghe and A. G. Suits, *J. Phys. Chem. Lett.*, 2017, **8**, 5153–5159.
82 C. Amarasinghe, C. A. Perera and A. G. Suits, *J. Chem. Phys.*, 2020, **152**, 184201.
83 P. G. Jambrina, D. Herráez-Aguilar, F. J. Aoiz, M. Sneha, J. Jankunas and R. N. Zare, *Nat. Chem.*, 2015, **7**, 661.
84 P. G. Jambrina, J. Aldegunde, F. J. Aoiz, M. Sneha and R. N. Zare, *Chem. Sci.*, 2016, **7**, 642.
85 M. Sneha, H. Gao, R. N. Zare, P. G. Jambrina, M. Menéndez and F. J. Aoiz, *J. Chem. Phys.*, 2016, **145**, 024308.
86 P. G. Jambrina, M. Menéndez and F. J. Aoiz, *Chem. Sci.*, 2018, **9**, 4837.
87 P. G. Jambrina, M. Menéndez, A. Zanchet, E. García and F. J. Aoiz, *Phys. Chem. Chem. Phys.*, 2019, **21**, 14012–14022.
88 R. J. Hinde, *J. Chem. Phys.*, 2008, **128**, 154308.
89 J. Zuo, J. F. E. Croft, Q. Yao, N. Balakrishnan and H. Guo, *J. Chem. Theory Comput.*, 2021, **17**, 6747–6756.
90 B. W. Bakr, D. G. A. Smith and K. Patkowski, *J. Chem. Phys.*, 2013, **139**, 144305.
91 F. Thibault, K. Patkowski, P. S. Żuchowski, H. Jóźwiak, R. Ciuryło and P. Wcisło, *J. Quant. Spectrosc. Radiat. Transf.*, 2017, **202**, 308.
92 Roueff, E. and Zeippen, C. J., *Astron. Astrophys. Suppl. Ser.*, 2000, **142**, 475–497.
93 J. L. Nolte, P. C. Stancil, T.-G. Lee, N. Balakrishnan and R. C. Forrey, *Astrophys. J.*, 2011, **744**, 62.
94 B. Zhou and M. Chen, *Mol. Phys.*, 2017, **115**, 2442–2450.
95 Y. Wang, J. Huang, W. Wang, T. Du, Y. Xie, Y. Ma, C. Xiao, Z. Zhang, D. H. Zhang and X. Yang, *Science*, 2023, **379**, 191–195.
96 H. da Silva, B. K. Kendrick and N. Balakrishnan, *J. Chem. Phys.*, 2022, **156**, 044305.
97 J. Jankunas, M. Sneha, R. N. Zare, F. Bouakline, S. C. Althorpe, D. Herráez-Aguilar and F. J. Aoiz, *Proc. Natl. Acad. Sci.*, 2014, **111**, 15–20.
98 J. Hazra, B. K. Kendrick and N. Balakrishnan, *J. Phys. B*, 2016, **49**, 194004.
99 B. K. Kendrick, J. Hazra and N. Balakrishnan, *J. Chem. Phys.*, 2016, **145**, 164303.
100 D. Yang, D. Xie and H. Guo, *J. Phys. Chem. Lett.*, 2022, **13**, 1777–1784.
101 M. H. Alexander and S. Stolte, *J. Chem. Phys.*, 2000, **112**, 8017–8026.
102 M. C. van Beek, J. J. ter Meulen and M. H. Alexander, *J. Chem. Phys.*, 2000, **113**, 637–646.
103 M. C. van Beek and J. J. ter Meulen, *J. Chem. Phys.*, 2001, **115**, 1843–1852.
104 A. Gijsbertsen, H. Linnartz, C. A. Taatjes and S. Stolte, *J. Am. Chem. Soc.*, 2006, **128**, 8777–8789.
105 M. J. L. de Lange, M. M. J. E. Drabbels, P. T. Griffiths, J. Bulthuis, S. Stolte and J. G. Snijders, *Chem. Phys. Lett.*, 1999, **313**, 491–498.
106 C. A. Taatjes, A. Gijsbertsen, M. J. L. de Lange and S. Stolte, *J. Phys. Chem. A*, 2007, **111**, 7631–7639.
107 B. Nichols, H. Chadwick, S. D. S. Gordon, C. J. Eyles, B. Hornung, M. Brouard, M. H. Alexander, F. J. Aoiz, A. Gijsbertsen and S. Stolte, *Chem. Sci.*, 2015, **6**, 2202–2210.
108 V. Walpole, C. G. Heid, P. G. Jambrina, F. J. Aoiz and M. Brouard, *J. Phys. Chem. A*, 2019, **123**, 8787–8806.
109 C. G. Heid, I. P. Bentham, V. Walpole, P. G. Jambrina, F. J. Aoiz and M. Brouard, *J. Phys. Chem. Lett.*, 2021, **12**, 310–316.
110 C. G. Heid, I. P. Bentham, V. Walpole, R. Gheorghe, P. G. Jambrina, F. J. Aoiz and M. Brouard, *Phys. Chem. Chem. Phys.*, 2020, **22**, 22289–22301.
111 C. G. Heid, I. P. Bentham, R. Gheorghe, P. G. Jambrina, F. J. Aoiz and M. Brouard, *Mol. Phys.*, 2022, **120**, e1946607.
112 T. R. Sharples, J. G. Leng, T. F. M. Luxford, K. G. McKendrick, P. G. Jambrina, F. J. Aoiz, D. W. Chandler and M. L. Costen, *Nat. Chem.*, 2018, **10**, 1148–1153.
113 S. A. Lahankar, J. Zhang, T. K. Minton and K. G. McKendrick, *J. Am. Chem. Soc.*, 2014, **136**, 12371–12384.
114 P. G. Jambrina, A. Zanchet, J. Aldegunde, M. Brouard and F. J. Aoiz, *Nat. Comm.*, 2016, **7**, 13439.
115 P. G. Jambrina, A. Zanchet, M. Menéndez, V. J. Herrero and F. J. Aoiz, *Phys. Chem. Chem. Phys.*, 2019, **21**, 25389.
116 F. Wang, J.-S. Lin and K. Liu, *Science*, 2011, **331**, 900–903.
117 F. Wang, K. Liu and T. Rakitzis, *Nat. Chem.*, 2012, **4**, 636–641.
118 F. Wang and K. Liu, *J. Chem. Phys.*, 2016, **145**, 144305.
119 F. Wang and K. Liu, *J. Chem. Phys.*, 2016, **145**, 144306.
120 H. Pan and K. Liu, *Phys. Chem. Chem. Phys.*, 2020, **22**, 10949–10956.
121 A. B. Henson, S. Gersten, Y. Shagam, J. Narevicius and E. Narevicius, *Science*, 2012, **338**, 234–238.
122 Y. Shagam, A. Klein, W. Skomorowski, R. Yun, V. Averbukh, C. P. Koch and E. Narevicius, *Nat. Chem.*, 2015, **7**, 921–926.

123 B. Margulis, K. P. Horn, D. M. Reich, M. Upadhyay, N. Kahn, A. Christianen, A. van der Avoird, G. C. Groenenboom, M. Meuwly, C. P. Koch and E. Narevicius, *Science*, 2023, **380**, 77–81.

124 A. Devolder, T. Tscherbul and P. Brumer, *Phys. Rev. A*, 2020, **102**, 031303.

125 A. Devolder, P. Brumer and T. V. Tscherbul, *Phys. Rev. Lett.*, 2021, **126**, 153403.

126 A. Devolder, T. V. Tscherbul and P. Brumer, *J. Phys. Chem. Lett.*, 2023, **14**, 2171–2177.

127 B. K. Kendrick, *Chem. Phys.*, 2018, **515**, 387–399.

128 B. K. Kendrick, *J. Phys. Chem. A*, 2019, **123**, 9919–9933.

129 K.-K. Ni, S. Ospelkaus, D. Wang, G. Quéméner, B. Neyenhuis, M. H. G. de Miranda, J. L. Bohn, J. Ye and D. S. Jin, *Nature*, 2010, **464**, 1324.

130 J.-R. Li, W. G. Tobias, K. Matsuda, C. Miller, G. Valtolina, L. De Marco, R. R. W. Wang, L. Lassablière, G. Quéméner, J. L. Bohn and J. Ye, *Nature Physics*, 2021, **17**, 1144–1148.

131 K. Matsuda, L. D. Marco, J.-R. Li, W. G. Tobias, G. Valtolina, G. Quéméner and J. Ye, *Science*, 2020, **370**, 1324–1327.

132 T. Karman and J. M. Hutson, *Phys. Rev. Lett.*, 2018, **121**, 163401.

133 L. Anderegg, S. Burchesky, Y. Bao, S. S. Yu, T. Karman, E. Chae, K.-K. Ni, W. Ketterle and J. M. Doyle, *Science*, 2021, **373**, 779–782.

134 H. Son, J. J. Park, Y.-K. Lu, A. O. Jamison, T. Karman and W. Ketterle, *Science*, 2022, **375**, 1006–1010.